

Substructure and dynamical state of 2092 rich clusters of galaxies derived from photometric data

Z. L. Wen^{*} and J. L. Han

National Astronomical Observatories, Chinese Academy of Sciences, 20A Datun Road, Chaoyang District, Beijing 100012, China

Accepted 2013 ... Received 2013 ...

ABSTRACT

Dynamical state of galaxy clusters is closely related to their observational properties in X-ray, optical and radio wavelengths. We develop a method to diagnose the substructure and dynamical state of galaxy clusters by using photometric data of Sloan Digital Sky Survey (SDSS). To trace mass distribution, the brightness distribution of member galaxies is smoothed by using a Gaussian kernel with a weight of their optical luminosities. After deriving the asymmetry, the ridge flatness and the normalized deviation of the smoothed optical map, we define a relaxation parameter, Γ , to quantify dynamical state of clusters. This method is applied to a test sample of 98 clusters of $0.05 < z \lesssim 0.42$ collected from literature with known dynamical states and can recognize dynamical state for relaxed ($\Gamma \geq 0$) and unrelaxed ($\Gamma < 0$) clusters with a success rate of 94%. We then calculate relaxation parameters of 2092 rich clusters previously identified from the SDSS, of which 28% clusters are dynamically relaxed with $\Gamma \geq 0$. We find that the dominance and absolute magnitude of the brightest cluster galaxies closely correlate with dynamical state of clusters. The emission power of radio halos is quantitatively related to cluster dynamical state, beside the known dependence on the X-ray luminosity.

Key words: galaxies: clusters: general

1 INTRODUCTION

Clusters of galaxies are the most massive bound systems in the universe. The hierarchical model (Peebles 1980) predicts that clusters of galaxies form by accretion and merging of smaller sub-clusters and groups (Colberg et al. 1999). Dynamical state of clusters can usually be divided into two broad classes, relaxed and unrelaxed. Determination of cluster dynamical state is important not only for understanding cluster properties in X-ray, optical and radio wavelengths (Santos et al. 2008; Feretti et al. 2012; Mann & Ebeling 2012) but also for cosmological studies (Smith et al. 2003; Puchwein & Bartelmann 2007; Comerford et al. 2010).

Dynamical state of a few hundred clusters has been diagnosed based on substructures in X-ray image and spectra data (e.g., Smith et al. 2005; Vikhlinin et al. 2005; Allen et al. 2008; Mann & Ebeling 2012), quantitatively by using the power ratio (e.g., Buote & Tsai 1995; Böhringer et al. 2010), the centroid shift (e.g., Mohr et al. 1995; Maughan et al. 2008; Mann & Ebeling 2012), the asymmetry and the concentration (e.g., Hashimoto et al. 2007; Santos et al. 2008). About 40%–70% of clusters show various substructures in X-ray images (e.g., Jones & Forman 1999; Schuecker et al. 2001; Smith et al. 2005) which are unrelaxed clusters undergone multiple merger events in the recent past

(Mann & Ebeling 2012). Relaxed clusters generally have cool cores of intracluster gas in the center (Edge et al. 1992; Allen et al. 2001; Bauer et al. 2005; Vikhlinin et al. 2005; Allen et al. 2008), and unrelaxed clusters are systematically hotter than relaxed clusters (Ota & Mitsuda 2002; Smith et al. 2005; Pedersen & Dahle 2007). Because the hydrostatic equilibrium is violated in unrelaxed clusters (Puchwein & Bartelmann 2007), clusters of various dynamical states have different scaling relations, e.g., between cluster mass and X-ray luminosity or temperature (Chen et al. 2007; Andrade-Santos et al. 2012).

Dynamical state is related to the cluster properties in radio (Burns et al. 1994; Bliton et al. 1998; Liuzzo et al. 2010). Almost all radio halos or radio relics were detected from unrelaxed merging clusters and mini-halo were usually found from relaxed clusters (Schuecker et al. 2001; Govoni et al. 2004; Cassano et al. 2010; Feretti et al. 2012).

In optical, three-dimensional distribution and motions of the member galaxies are the most direct tracer of dynamical state of clusters. Spectroscopic surveys of member galaxies are powerful to reveal substructures along the line of sight (Dressler & Shectman 1988). Relaxed clusters should have a Gaussian distribution for redshifts of member galaxies, and non-Gaussian redshift distribution is a clear evidence of unrelaxed state (Colless & Dunn 1996; Halliday et al. 2004). Previously substructures were searched from the spectroscopic data by many methods, e.g., the Δ -statistics which measures the deviations of the local radial velocity distri-

^{*} E-mail: zhonglue@nao.cas.cn

bution from the global values (Dressler & Shectman 1988), the hierarchical clustering method (Serna & Gerbal 1996), the skewness and kurtosis of velocity distributions (West & Bothun 1990; Solanes et al. 1999), the Anderson–Darling, Kolmogorov and χ^2 tests (Hou et al. 2009) and multidimensional normal mixture modelling (Einasto et al. 2010). About 30%–70% of clusters have substructures shown in spectroscopic data (Dressler & Shectman 1988; West & Bothun 1990; Hou et al. 2009; Aguerri & Sánchez-Janssen 2010; Einasto et al. 2012; Hou et al. 2012).

However, spectroscopic observations usually are incomplete for cluster member galaxies especially for faint galaxies and only available for a very limited sample of galaxy clusters. Projected two-dimensional distributions of member galaxies were also used to search for substructures by, e.g., tests of the asymmetry, the angular separation and density contrast (West et al. 1988), cluster centroid shift (Kolokotronis et al. 2001), the adaptive-kernel based DEDICA algorithm (Pisani 1993; Ramella et al. 2007), the average two-point correlation function statistic (Salvador-Sole et al. 1993) and wavelet analysis (Flin & Krywult 2006). These two-dimensional approaches work on positions of member galaxies and have been applied to nearby clusters, which show that 30%–70% of clusters have substructures (e.g., Flin & Krywult 2006; Ramella et al. 2007).

Up to now, more than 130 000 clusters have been identified from optical data, e.g., from the Sloan Digital Sky Survey (SDSS) (Wen et al. 2009; Hao et al. 2010; Szabo et al. 2011; Wen et al. 2012) and thousands from X-ray data, e.g., from the *ROSAT* survey (Böhringer et al. 2000a, 2004). Only a few hundred nearby clusters have their substructures quantified from X-ray image or optical spectrometry (e.g., Dressler & Shectman 1988; Buote & Tsai 1995; Weißmann et al. 2013). The challenge for quantifying dynamical state of a large sample of clusters is to obtain deep X-ray observations or complete optical spectroscopic redshifts of member galaxies.

In this paper, we develop a method to diagnose two-dimensional substructures and dynamical states of galaxy clusters by using multi-band optical photometric data, and quantify dynamical states for a large sample of rich clusters. By using SDSS photometric redshifts, we can identify luminous member galaxies of clusters with reasonable completeness and diminish most contamination from foreground and background galaxies (Wen et al. 2009). Because more luminous member galaxies trace more mass, the projected distribution of member galaxies in the sky plane weighted with optical luminosity can well trace the projected light and mass distribution of galaxy clusters (Zitrin et al. 2012a,b). Very relaxed clusters should have a very smooth symmetrical mass and light distribution, while the unrelaxed clusters should have substructures. To verify the method for quantification of dynamical states from optical data, in Section 2 we collect a test sample of rich clusters from literature with dynamical states classified as relaxed and unrelaxed based on X-ray, optical and radio data, and we obtain their optical data from SDSS. In Section 3, we describe the method and define a relaxation parameter to quantify cluster dynamical state based on the smoothed optical map for the brightness distribution of member galaxies. We apply the method to the test cluster sample, and find that the known relaxed and unrelaxed clusters can be well distinguished with a success rate of 94%. In Section 4, we calculate the relaxation parameters for 2092 rich clusters ($0.05 < z \leq 0.42$) taken from the catalog of Wen et al. (2012) which were identified from optical photometric data of the SDSS-III. The correlations between the relaxation parameter and cluster properties are discussed. We present our conclusions in Section 5.

Throughout this paper, we assume a Λ CDM cosmology, taking $H_0 = 100 h \text{ km s}^{-1} \text{ Mpc}^{-1}$, with $h = 0.72$, $\Omega_m = 0.3$ and $\Omega_\Lambda = 0.7$.

2 TEST SAMPLE OF GALAXY CLUSTERS WITH KNOWN DYNAMICAL STATES

We collect the test sample of clusters with known dynamical states to verify the method for quantification of dynamical states of clusters by using optical photometric data and to find optimized parameters.

2.1 Sample collection

Galaxy clusters have been broadly classified as dynamically ‘relaxed’ and ‘unrelaxed’. In literature, a few hundreds of clusters have their dynamical states so classified according to their X-ray characteristics or redshift distributions of member galaxies (e.g., Czoske et al. 2002; Vikhlinin et al. 2005; Cypriano et al. 2005; Allen et al. 2008; Mann & Ebeling 2012), which we have collected into the parent sample. We also collect the clusters based on X-ray and radio observations. Most clusters with a cool core in X-ray are known to be relaxed (Edge et al. 1992; Allen et al. 2001; Bauer et al. 2005; Vikhlinin et al. 2005). Therefore, clusters are collected as relaxed clusters if they have a central cooling time less than 1 Gyr (Hicks et al. 2010; Wang et al. 2010) or a cooling time less than 10 Gyr within a radius greater than 50 kpc (Allen 2000; Bauer et al. 2005), except for a few cool-core clusters with distinct disturbed X-ray morphologies (e.g., A85 and A115, Kempner et al. 2002; Durret et al. 2005; Gutierrez & Krawczynski 2005; Bauer et al. 2005) which we classify as unrelaxed clusters. Clusters with radio halos or radio relics are exclusively unrelaxed systems (e.g., Govoni et al. 2004; Barrena et al. 2007, 2009; Boschini et al. 2009; Cassano et al. 2010). As long as radio halo/relics were detected (Venturi et al. 2008; Cohen & Clarke 2011; Feretti et al. 2012; Nuza et al. 2012), we collect the clusters into the parent sample as unrelaxed clusters.

From the parent sample with properly known dynamical states for relaxed and unrelaxed clusters, we choose the test sample of clusters only in the sky area of SDSS-III so that we can get their optical data for member galaxies. To ensure the complete detection of luminous member galaxies (Wen et al. 2012), we further limit the cluster sample to be in the redshift range of $0.05 < z \lesssim 0.42$. We also set the threshold of cluster richness (defined below) $R_{L*} \geq 50$ so that the test clusters have enough recognized member galaxies. With these selection criteria, we get the test sample of 98 clusters with known dynamical states, including 35 relaxed and 63 unrelaxed clusters, as listed in Table 1. Among the 35 relaxed clusters, 24 have been classified in literature already (see references in Table 1), 11 clusters are included because of their cool cores shown in X-ray. Among 63 unrelaxed clusters, 54 clusters have their classification made previously in literature and 9 clusters are included because of their radio halos or relics.

2.2 Member galaxies discrimination and richness estimation

For the test sample of 98 clusters and also the work sample of 2092 clusters for Section 4.1, we use the photometric data of the SDSS

Table 1. Test sample of clusters with known dynamical states in the field of SDSS-III

Name	R.A.	Dec.	z	r_{BCG}	r_{200}	R_{L*}	N_{200}	Γ	Comment and reference
(1)	(deg)	(deg)	(4)	(5)	(Mpc)	(7)	(8)	(9)	(10)
RXC J0003.8+0203	0.95698	2.06647	0.0978	14.09	1.57	70.32	46	0.28 ± 0.04	R, relaxed[wbs+13]
A13	3.41056	-19.50015	0.0943	14.61	1.78	76.22	46	-0.46 ± 0.09	U, merger[jsc+08],radio[fgg+12]
CL0024.0+1652	6.64862	17.16197	0.3871	17.74	1.87	94.77	72	0.49 ± 0.04	U, merger (line of sight)[cmk+02]
A68	9.27851	9.15670	0.2861	16.72	1.96	107.22	76	-0.50 ± 0.10	U, merger[st08]
A85	10.46029	-9.30313	0.0554	13.31	1.68	81.23	67	-0.91 ± 0.09	U, merger,cool[ksr02],radio[fgg+12]
A2813	10.85232	-20.62496	0.2924	17.15	2.00	133.15	74	-0.24 ± 0.04	U, merger[me12]
A98	11.60318	20.62172	0.1028	14.75	1.75	115.93	98	-0.69 ± 0.10	U, merger[bro+94]
A115	14.00108	26.34230	0.1920	16.44	2.05	134.95	104	-0.76 ± 0.11	U, merger[fb+81],radio[fgg+12],cool[bfs+05]
MACS J0140.0-0555	25.00334	-5.91744	0.4474	18.42	1.76	92.27	68	0.00 ± 0.08	U, merger[me12]
A267	28.17485	1.00709	0.2297	15.59	1.92	130.44	105	0.48 ± 0.02	U, merger[sk+05]
MACS J0159.8-0849	29.95555	-8.83303	0.4052	17.82	1.71	104.64	86	0.22 ± 0.05	R, relaxed[ars+08]
A370	39.96969	-1.57192	0.3732	17.73	2.18	183.49	139	0.07 ± 0.06	U, merger[omf98]
A383	42.01413	-3.52923	0.1883	15.94	1.71	100.85	70	0.41 ± 0.04	R, relaxed[ars+08],cool[zfb+07]
RX J0256.5+0006	44.12854	0.10091	0.3665	18.04	1.58	62.74	48	-1.81 ± 0.13	U, merger[mnr+04]
A586	113.08453	31.63353	0.1710	14.76	1.90	160.23	126	0.43 ± 0.02	R, relaxed[cls+05],cool[bfs+05]
A611	120.23675	36.05654	0.2873	16.66	1.79	107.64	83	0.11 ± 0.06	R, relaxed[ars+08]
A644	124.35672	-7.51257	0.0705	14.01	1.62	77.30	48	-0.49 ± 0.07	U, merger[bhs05]
RXC J0821.8+0112	125.46104	1.19709	0.0871	14.98	1.58	63.22	44	-0.47 ± 0.10	U, merger[wbs+13]
A665	127.73873	65.84197	0.1830	16.25	2.07	208.30	178	-0.26 ± 0.10	U, merger[mv01],radio[fgg+12]
MS0839.8+2938	130.73311	29.45750	0.1937	16.34	1.37	52.05	46	0.37 ± 0.03	R, cool[hmd10]
A697	130.73982	36.36646	0.2823	17.53	1.44	51.64	64	-0.22 ± 0.06	U, merger (line of sight)[gbb06],radio[fgg+12]
Z1953	132.53297	36.07046	0.3764	18.33	2.02	113.13	111	-0.36 ± 0.06	U, merger[me12]
A750	137.30312	10.97475	0.1763	15.56	2.00	148.73	151	0.19 ± 0.05	R, cool[bfs+05]
A746	137.37737	51.51784	0.2320	17.91	1.68	85.48	81	-2.49 ± 0.10	U, radio[fgg+12]
IRAS 09104+4109	138.43956	40.94117	0.4408	18.17	1.50	58.35	40	0.40 ± 0.03	R, cool[all00]
A773	139.47258	51.72710	0.2173	16.08	2.13	149.40	134	-0.12 ± 0.07	U, merger[bbg+07],radio[fgg+12]
A781	140.20116	30.47176	0.2881	17.04	1.85	172.82	127	-0.61 ± 0.07	U, merger[shw+08],radio[fgg+12]
A800	142.15269	37.78979	0.2450	17.12	1.94	106.21	79	-0.21 ± 0.07	U, radio[gff+12]
A851	145.73941	46.98050	0.4069	18.43	1.63	86.69	69	-1.15 ± 0.05	U, merger[dsc03],radio[fgg+12]
Z2701	148.20488	51.88484	0.2152	16.09	1.64	69.09	52	0.25 ± 0.03	R, cool[bfs+05]
A910	150.76340	67.17450	0.2304	16.28	2.19	214.95	116	-0.45 ± 0.08	U, radio[gff+12]
MACS J1006.9+3200	151.72778	32.02545	0.3983	17.85	1.67	68.02	59	-0.59 ± 0.10	U, merger[me12]
A963	154.26514	39.04706	0.2056	15.93	1.69	60.56	66	0.05 ± 0.04	R, relaxed[ars+08],cool[all00]
A959	154.39302	59.56106	0.2880	17.76	1.87	104.91	80	-1.12 ± 0.06	U, merger[bbg09]
Z3146	155.91515	4.18629	0.2898	16.84	1.41	60.82	47	0.39 ± 0.02	R, relaxed[ars+08],cool[all00]
A1201	168.22708	13.43584	0.1681	15.23	1.71	95.73	78	-0.16 ± 0.10	U, merger[onc+09]
MACS J1115.8+0129	168.96626	1.49863	0.3520	17.68	1.51	54.71	51	0.42 ± 0.04	R, relaxed[ars+08]
A1240	170.90714	43.05779	0.1957	16.56	1.54	84.65	66	-0.52 ± 0.12	U, merger[bbg+09],radio[fgg+12]
A1278	172.53789	20.51503	0.1300	15.44	1.86	108.42	90	-0.29 ± 0.10	U, merger[mol+03]
A1351	175.60326	58.53488	0.3229	17.07	2.21	130.13	94	-1.23 ± 0.15	U, merger[hds09],radio[fgg+12]
A1413	178.82501	23.40494	0.1429	14.52	1.82	100.78	90	0.36 ± 0.02	R, relaxed[ars+08],cool[all00]
A1423	179.32217	33.61094	0.2130	16.13	1.62	79.82	77	0.16 ± 0.03	R, cool[bfs+05]
A1550	187.26057	47.62238	0.2540	17.03	2.06	136.44	111	-0.42 ± 0.09	U, radio[gff+12]
A1560	188.47086	15.19464	0.2835	17.47	1.36	68.35	54	-0.74 ± 0.09	U, merger[uc82]
A1589	190.32281	18.57457	0.0704	13.96	1.81	101.94	71	-0.61 ± 0.13	U, merger[bro+94]
A1612	191.97337	-2.80733	0.1819	16.33	1.91	111.88	81	-1.71 ± 0.12	U, radio[fgg+12]
A1650	194.67290	-1.76146	0.0839	14.08	1.51	75.02	51	0.21 ± 0.03	R, cool[dvo+05]
A1682	196.70831	46.55927	0.2257	16.16	2.04	126.85	115	-0.87 ± 0.06	U, merger[mol+03],radio[vgd+08]
ZwCl1305.4+2941	196.95512	29.43006	0.2405	16.14	1.41	55.94	38	0.48 ± 0.03	R, relaxed[gtv+08]
A1689	197.87291	-1.34109	0.1828	15.69	2.28	172.53	156	0.47 ± 0.05	U, merger[am04],radio[fgg+12],cool[all00]
A1704	198.60248	64.57538	0.2191	16.50	1.63	88.00	64	0.00 ± 0.06	R, cool[all00]
A1703	198.77182	51.81738	0.2836	16.76	1.96	130.12	100	0.16 ± 0.04	R, relaxed[rpl+09]
A1750	202.79594	-1.72730	0.0835	14.47	1.85	134.22	83	-0.09 ± 0.04	U, merger[djt+01],bbs+04]
A1758	203.16005	50.56000	0.2794	17.33	1.98	155.02	129	-0.70 ± 0.08	U, merger[dk04],radio[fgg+12]
A1763	203.83372	41.00115	0.2278	16.37	1.96	155.64	146	0.13 ± 0.05	U, merger[st08]
A1795	207.21877	26.59293	0.0633	13.67	1.50	51.87	51	0.36 ± 0.05	R, relaxed[ars+08],cool[all00]
MS1358.4+6245	209.96069	62.51819	0.3271	17.77	1.72	85.96	75	-0.69 ± 0.10	U, merger[fff+98],cool[all00]
A1835	210.25864	2.87847	0.2520	16.06	2.22	192.81	178	0.56 ± 0.02	R, relaxed[ars+08],cool[all00]
A1904	215.54253	48.57074	0.0710	13.77	1.75	102.75	68	-0.49 ± 0.12	U, merger[blw+96]
A1914	216.48611	37.81646	0.1700	15.62	2.03	135.55	117	-0.36 ± 0.10	U, merger[gm+04],radio[fgg+12]
MaxBCG J217.9+13.5	217.95869	13.53471	0.1599	15.40	1.44	50.58	32	-0.15 ± 0.05	U, radio[nhv 12]
A1942	219.59111	3.67035	0.2247	16.25	1.55	81.55	71	0.24 ± 0.04	R, relaxed[cpl+08]
A1995	223.23949	58.04876	0.3212	17.71	1.80	83.59	83	-0.09 ± 0.07	U, radio[fgg+12]
A1991	223.63121	18.64232	0.0592	13.61	1.59	68.09	51	-0.41 ± 0.05	R, relaxed[yvm+05],cool[wok+10]
Z7160	224.31294	22.34289	0.2576	16.37	1.66	78.77	54	0.22 ± 0.04	R, cool[all00]
RXC J1504.1-0248	226.03130	-2.80460	0.2169	16.27	1.68	80.30	66	0.32 ± 0.04	R, relaxed[ars+08],cool[wok+10]
A2034	227.54880	33.48647	0.1116	14.75	1.89	116.63	89	-0.25 ± 0.06	U, merger[ksm03],radio[fgg+12]
A2029	227.73376	5.74478	0.0779	13.36	1.71	87.42	91	0.40 ± 0.03	R, relaxed[ars+08],cool[all00]
A2048	228.80881	4.38622	0.0950	15.21	1.64	71.28	72	-0.74 ± 0.07	U, radio[fgg+12]

Table 1. *continued*

Name	R.A. (deg)	Dec. (deg)	z	r_{BCG}	r_{200} (Mpc)	R_{L*}	N_{200}	Γ	Comments and reference
(1)	(2)	(3)	(4)	(5)	(6)	(7)	(8)	(9)	(10)
RXC J1516.5–0056	229.24202	−1.11080	0.1186	15.29	1.29	61.43	49	$−1.24 \pm 0.10$	U, merger[wbs+13]
A2061	230.33575	30.67093	0.0788	13.99	1.86	87.42	90	$−0.58 \pm 0.11$	U, merger[mbz+04],radio[fgg+12]
A2065	230.60008	27.71437	0.0726	14.84	1.90	102.58	113	$−0.53 \pm 0.07$	U, merger[msv99]
A2069	231.03093	29.88896	0.1135	14.89	1.80	114.07	114	$−0.26 \pm 0.04$	U, merger[onc+09]
RX J1532.9+3021	233.22408	30.34984	0.3621	17.34	1.60	74.22	59	0.28 ± 0.04	R, relaxed[ars+08],cool[bfs+05]
A2111	234.91873	34.42424	0.2280	16.95	2.03	134.29	131	$−0.04 \pm 0.05$	U, merger[wul97]
A2142	239.58333	27.23341	0.0910	14.40	2.03	140.29	154	$−0.31 \pm 0.06$	U, merger[mpn+00],cool[all00]
MS1621.5+2640	245.89771	26.57057	0.4270	18.69	1.61	77.81	67	$−0.59 \pm 0.04$	U, merger[scf+10]
A2219	250.08255	46.71153	0.2244	16.54	1.85	148.59	148	$−0.24 \pm 0.06$	U, merger[bgb+04],radio[fgg+12]
A2244	255.67706	34.06000	0.0994	14.02	1.76	65.80	81	0.48 ± 0.03	R, cool[dvo+05]
A2256	256.11325	78.64049	0.0594	13.28	1.71	67.64	42	$−0.17 \pm 0.08$	U, merger[smm+02],radio[fgg+12]
A2255	258.11984	64.06083	0.0808	13.97	2.14	139.88	111	$−1.02 \pm 0.10$	U, merger[brp+95],radio[fgg+12]
A2259	260.04019	27.66889	0.1640	15.26	1.36	53.46	45	0.36 ± 0.03	R, cool[bfs+05]
RX J1720.1+2638	260.04184	26.62557	0.1601	15.51	1.54	70.83	60	0.33 ± 0.03	R, relaxed[onc+09],cool[bfs+05]
MACS J1720.3+3536	260.06989	35.60736	0.3913	17.85	1.62	79.19	62	0.02 ± 0.05	R, relaxed[ars+08],cool[wok+10]
A2261	260.61325	32.13257	0.2233	15.26	2.18	219.92	176	0.25 ± 0.03	R, cool[all00]
MACS J1731.6+2252	262.91638	22.86628	0.3660	17.72	2.07	123.13	88	$−0.41 \pm 0.10$	U, merger[me12],radio[bbv+12]
RX J2129.6+0006	322.41647	0.08921	0.2339	16.32	1.65	84.41	61	0.42 ± 0.04	R, relaxed[ars+08],cool[bfs+05]
A2356	323.94287	0.11587	0.1175	15.91	1.49	50.95	40	$−1.90 \pm 0.09$	U, merger[uc82]
A2390	328.40347	17.69548	0.2302	16.66	1.87	104.12	107	0.04 ± 0.06	R, relaxed[ars+08],cool[all00]
RXC J2157.4–0747	329.25717	−7.83959	0.0583	13.97	1.54	63.38	45	$−1.36 \pm 0.11$	U, merger[wbs+13]
A2440	335.98724	−1.58326	0.0900	14.38	1.88	78.46	52	$−0.44 \pm 0.10$	U, merger[msb+11]
A2443	336.53302	17.35651	0.1070	14.64	1.77	97.42	69	$−1.20 \pm 0.10$	U, radio[cc11]
MACS J2228.5+2036	337.14050	20.62120	0.4120	18.64	1.95	153.70	109	$−0.89 \pm 0.12$	U, merger[me12]
MACS J2243.3–0935	340.83633	−9.58858	0.4393	19.76	1.83	93.70	93	$−1.53 \pm 0.07$	U, merger[me12]
A2537	347.09262	−2.19217	0.2950	16.79	2.13	107.27	101	0.06 ± 0.05	R, relaxed[ars+08]
A2626	354.12756	21.14734	0.0546	13.17	1.56	66.98	47	0.07 ± 0.05	R, relaxed[wbs+13]
A2631	354.41553	0.27137	0.2772	17.24	1.75	97.17	91	$−0.02 \pm 0.10$	U, merger[me12]
ZwCl2341.1+0000	355.94806	0.25666	0.2673	17.99	1.66	104.48	75	$−0.56 \pm 0.08$	U, merger[ak13],radio[nhv+12]

Note. Column (1): cluster name. Column (2)–(4): R.A., Dec. (J2000) and redshift of cluster. Column (5): r -band magnitude of BCG. Column (6): cluster radius, r_{200} (Mpc). Column (7): cluster richness. Column (8): number of member galaxies within r_{200} . Column (9): relaxation parameter. Comments in column (10): ‘R/U’ refers to classification (relaxed/unrelaxed) of clusters in this work. ‘merger’ means the cluster shows merging signatures; ‘radio’ means the cluster has radio halo/relic; ‘cool’ means the cluster has a cool core in X-ray. Reference for ‘merger’, ‘radio’ and ‘cool’ in column (10): ak13 (Akamatsu & Kawahara 2013); all00 (Allen 2000); am04 (Andersson & Madejski 2004); ars+08 (Allen et al. 2008); bbg+07 (Barrena et al. 2007); bbg09 (Boschin et al. 2009); bbv+12 (Bonafede et al. 2012); bfs+05 (Bauer et al. 2005); bgb+04 (Boschin et al. 2004); bgb+09 (Barrena et al. 2009); bhs05 (Buote et al. 2005); blw+96 (Baier et al. 1996); bps+04 (Belsole et al. 2004); bro+94 (Burns et al. 1994); brp+95 (Burns et al. 1995); cc11 (Cohen & Clarke 2011); cls+05 (Cypriano et al. 2005); cmk+02 (Czoske et al. 2002); cpl+08 (Capelato et al. 2008); dfj+01 (Donnelly et al. 2001); dk04 (David & Kempner 2004); dsc03 (De Filippis et al. 2003); dvo+05 (Donahue et al. 2005); fbb+81 (Forman et al. 1981); fff+98 (Fisher et al. 1998); fgg+12 (Feretti et al. 2012); gbb06 (Girardi et al. 2006); gff+12 (Govoni et al. 2012); gmv+04 (Govoni et al. 2004); gtv+08 (Gastaldello et al. 2008); hmd10 (Hicks et al. 2010); hsd09 (Holhjem et al. 2009); jsc+08 (Juett et al. 2008); ksm03 (Kempner et al. 2003); ksr02 (Kempner et al. 2002); mbz+04 (Marini et al. 2004); me12 (Mann & Ebeling 2012); mnr+04 (Majerowicz et al. 2004); mol+03 (Morrison et al. 2003); mpn+00 (Markevitch et al. 2000); msb+11 (Maurogordato et al. 2011); msv99 (Markevitch et al. 1999); mv01 (Markevitch & Vikhlinin 2001); nhv+12 (Nuza et al. 2012); omf98 (Ota et al. 1998); onc+09 (Owers et al. 2009); rpl+09 (Richard et al. 2009); shw+08 (Sehgal et al. 2008); sks+05 (Smith et al. 2005); smm+02 (Sun et al. 2002); scf+10 (Shan et al. 2010); st08 (Smith & Taylor 2008); uc82 (Ulmer & Cruddace 1982); vgd+08 (Venturi et al. 2008); vmm+05 (Vikhlinin et al. 2005); wbs+13 (Weißmann et al. 2013); wok+10 (Wang et al. 2010); wul97 (Wang et al. 1997); zfb+07 (Zhang et al. 2007).

Data Release 8¹ (SDSS DR8, Aihara et al. 2011) to discriminate luminous member galaxies and to estimate cluster richness and radius which will be used in the quantification of cluster dynamical state. If any objects in the SDSS DR8 have deblending problems and saturated, they are discarded using the flags².

In our work, the location of the first brightest cluster galaxy (BCGs) identified from optical photometric data is taken as the cluster center. This is reasonable because for clusters with X-ray

emission, Wen et al. (2009) showed that most of the first BCGs have a projected separation less than 0.2 Mpc from the X-ray peaks.

Luminous member galaxy candidates of a cluster are selected according to photometric redshifts (hereafter photo- z s) and the projected separation from the center. The uncertainties of photo- z s are $\sigma_z \sim 0.025\text{--}0.030$ in the redshift range of $z < 0.45$ (Wen et al. 2012). We assume that the uncertainty increases with redshift in the form of $\sigma_z = \sigma_0(1+z)$ for all galaxies. Member galaxy candidates brighter than $M_r^e(z) \leq -20.5$ are selected from SDSS data within a photo- z slice of $z \pm 0.04(1+z)$. Here, M_r^e is the evolution-corrected absolute magnitude in the r band, $M_r^e(z) = M_r(z) + Qz$, where we adopt a passive evolution of $Q = 1.62$ (Blanton et al. 2003). The completeness of such selected member galaxies is more

¹ <http://www.sdss3.org/dr8/>

² (flags & 0x20) = 0 and (flags & 0x80000) = 0 and ((flags & 0x400000000000) = 0 or psfmagerr_r <= 0.20) and ((flags & 0x40000) = 0)

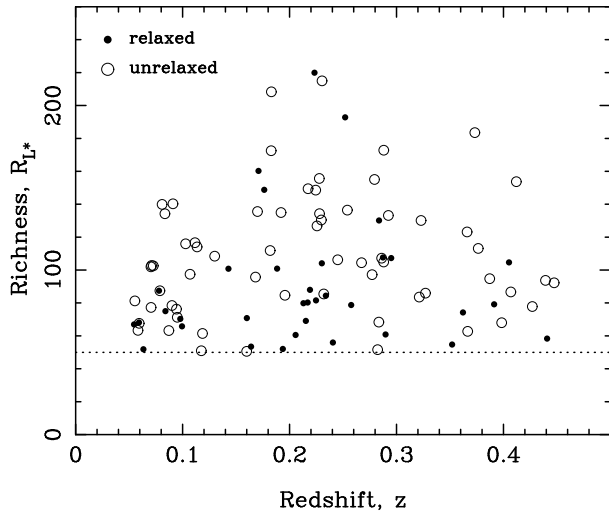


Figure 1. Richness distribution of the test sample of 98 clusters with known dynamical states in the redshift range of $0.05 < z \lesssim 0.42$. 35 relaxed clusters are plotted as black dots, and 63 unrelaxed clusters are plotted as open circles. The dotted line indicates $R_{L^*} = 50$.

than 90% for rich clusters (Wen et al. 2009). Objects with a large photo- z error, $z_{\text{Err}} > 0.08(1+z)$, are discarded for member galaxy candidates because they suffer bad photometry or contamination of stars. In this thick redshift slice, the relatively large uncertainty of photo- z leads to member galaxy candidates contaminated by foreground and background galaxies. To further diminish the contamination and incompleteness, we complement the photometric redshift with the spectroscopic measurements of the SDSS DR9 (Ahn et al. 2012). Member galaxy candidates within the projected separation < 2 Mpc from the cluster center are discarded from the list if they have a velocity difference $\Delta v > 2500$ km s $^{-1}$ from cluster redshift. For completeness, we include the missing galaxies in the photo- z data if they have a velocity difference $\Delta v \leq 2500$ km s $^{-1}$ from the cluster redshift and a separation of < 2 Mpc from the cluster center.

Cluster radius and richness are estimated from this list of member galaxy candidates by using the procedure of Wen et al. (2012). For each cluster, we first get the sum of the r band luminosities of member galaxies within a photo- z slice of $z \pm 0.04(1+z)$ and within 1 Mpc from the cluster center, $L_{1\text{Mpc}}$, with a local background subtracted³. We then relate $L_{1\text{Mpc}}$ to cluster radius, r_{200} , i.e., the radius within which the mean density of a cluster is 200 times of the critical density of the universe, by using the relation (Wen et al. 2012)

$$\log r_{200} = -0.57 + 0.44 \log(L_{1\text{Mpc}}/L^*), \quad (1)$$

where r_{200} is in units of Mpc, L^* is the evolved characteristic luminosity of galaxies in the r band, defined as $L^*(z) = L^*(z=0)10^{0.4Qz}$ (Blanton et al. 2003). The r -band total luminosity L_{200} are then obtained from the sum of r -band luminos-

³ To estimate local background, we follow the method of Popesso et al. (2004) and divide the annulus between 2 and 4 Mpc for each cluster around the BCG into 48 sections with an equal area. Within the same magnitude and photo- z range, we calculate the r -band total luminosity in each section and estimate the mean value and its root mean square. The regions with luminosities larger than 3σ are discarded and the mean is recalculated and taken as the local background.

ity of cluster members within the radius of r_{200} . The cluster richness is thus defined as $R_{L^*} = L_{200}/L^*$. For the test sample, we include rich clusters with $R_{L^*} \geq 50$, which corresponds to $M_{200} \geq 3.15 \times 10^{14} M_{\odot}$ according to equation 2 of Wen et al. (2012). The radius and richness for 98 test clusters are listed in Table 1, and their distribution across redshift and richness is plotted in Fig. 1.

3 QUANTIFICATION OF CLUSTER DYNAMICAL STATES FROM PHOTOMETRIC DATA

We quantify substructures of the two-dimensional optical maps for dynamical states of clusters by using the two-dimensional brightness distribution of cluster member galaxies. Because more luminous member galaxies can trace more mass, all member galaxies selected above for each cluster are smoothed and weighted by their luminosities with a Gaussian kernel to get the brightness distribution of a cluster in the sky plane. We then calculate three quantities defined in the following subsections: the asymmetry factor, α , the ridge flatness, β , and the normalized deviation, δ , to quantify the dynamical states of clusters. Considering that the contamination rate of member galaxies increases with cluster centric distance, we work on the smoothed optical luminosity distribution within the central region of clusters within $r_{500} = 2/3 r_{200}$ (Shimizu et al. 2003) for dynamical state of clusters. The value of r_{200} is estimated by using Equation (1).

3.1 The smoothed optical map

From SDSS-III, we get the r -band positions and luminosities of member galaxies of a cluster within a photo- z slice of $z \pm 0.04(1+z)$ and a radius of r_{200} . The first step to quantify the dynamical state is to smooth the optical photometric data with a two-dimensional Gaussian function. Positions (RA, Dec.) of galaxies are transformed into Cartesian coordinates (x, y) centering on the cluster center. In practice, the region of 4 Mpc \times 4 Mpc is divided into 200 pixels \times 200 pixels, so that each pixel has a linear size of 20 kpc. The optical luminosity within each pixel (x_i, y_j) can be calculated by convolving all member galaxies with a Gaussian kernel,

$$I(x_i, y_j) = \sum_{k=1}^{N_{200}} L_k g(x_i - x_k, y_j - y_k, \sigma_k), \quad (2)$$

where x_k and y_k are the coordinates of the k th member galaxy, L_k is the r -band luminosity of this galaxy in unit of L^* , N_{200} is the total number of member galaxies within a region of a photo- z slice of $z \pm 0.04(1+z)$ and a radius of r_{200} , $g(x, y, \sigma)$ is a two-dimensional Gaussian function with a smooth scale of σ ,

$$g(x, y, \sigma) = \frac{1}{2\pi\sigma^2} \exp\left(-\frac{x^2 + y^2}{2\sigma^2}\right). \quad (3)$$

It has been shown that light-to-mass ratios vary with cluster centric distance (Katgert et al. 2004; Medezinski et al. 2010). The luminosities of member galaxies at different radii are therefore related to galaxy mass with various light-to-mass ratios, so that they contribute to dynamical state with different smooth scale. Here, we take a smooth scale in the form of

$$\frac{\sigma}{r_{200}} = \left(\sigma_a + \sigma_b \frac{r}{r_{200}}\right), \quad (4)$$

where σ_a and σ_b are the two parameters for smooth scale, r/r_{200} is projected distance of a member galaxy from the cluster center

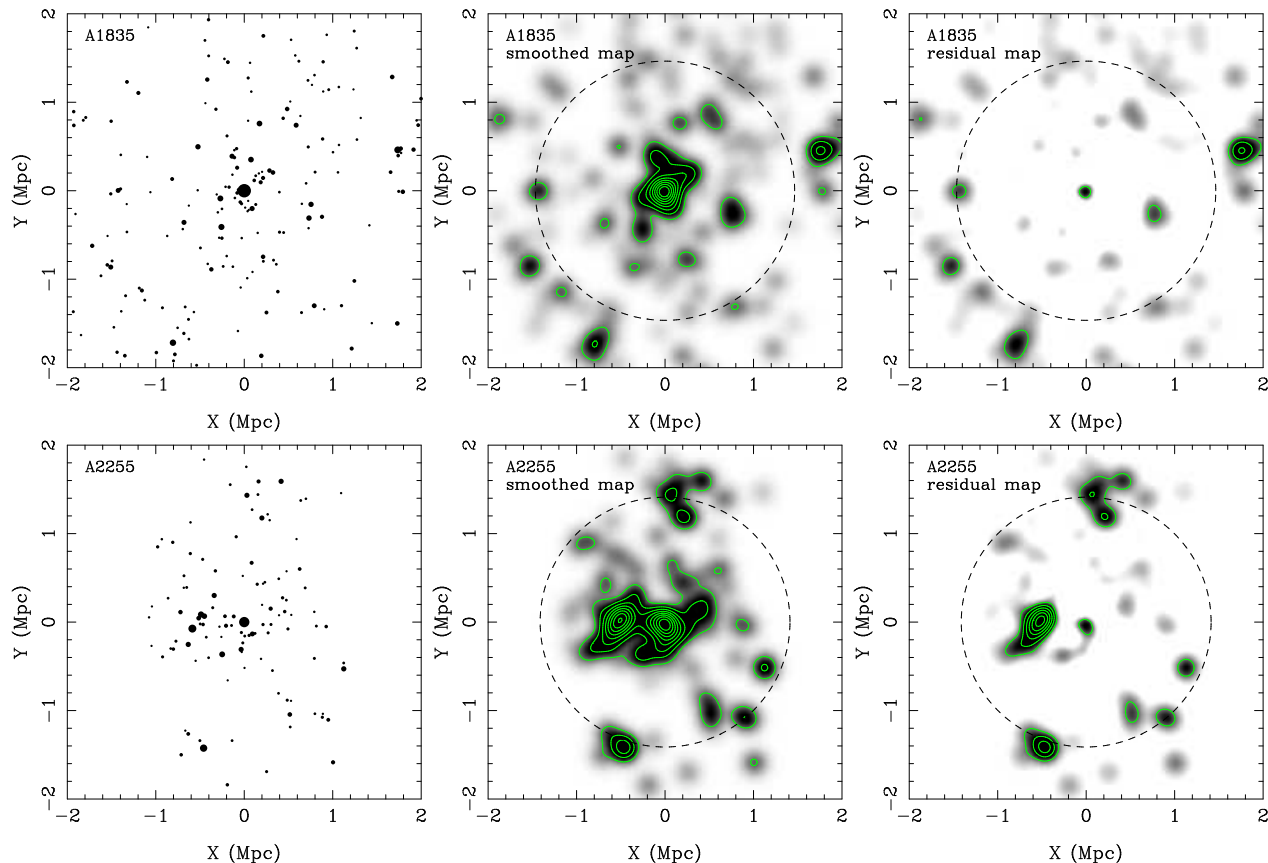


Figure 2. Projected distributions of member galaxies for a relaxed cluster, A1835 (upper panels), and a merging cluster, A2255 (lower panels). In the left panels, the black dots show the positions and the weight of galaxy luminosity (L_r) with the symbol size scaled by $\sqrt{L_r/L^*}$. The middle panels are the smoothed brightness maps of member galaxies convolved by a Gaussian function in Equation (3) with $\sigma = 0.05r_{200}$. The right panels are the residual maps after the smoothed map being subtracted by the best-fitting two-dimensional King model. The dashed circles indicate the regions with a radius of $r_{500} = 2/3 r_{200}$.

in unit of r_{200} . Richer clusters have larger r_{200} and are smoothed with larger scales. This ensures that our calculations below are independent of cluster radius or richness. The background is subtracted as described above to give a net two-dimensional smoothed brightness map of a cluster. Two examples are shown in Fig. 2 for the projected luminosity distributions of member galaxies (left panels), and the smoothed maps (middle panels) and the residual maps (right panels, after subtraction of the best-fitting two-dimensional King model, see discussions below) for a relaxed cluster, A1835, and a merging cluster, A2255. The values of σ_a and σ_b will be optimized in following calculations for dynamical states of clusters.

3.2 Asymmetry factor, α

A relaxed cluster has a regular symmetrical morphology, while an unrelaxed cluster shows many substructures. The asymmetry of galaxy distribution can be used to quantify the substructure of clusters. For example, as shown in the middle panel of Fig. 2, the relaxed cluster, A1835, has a much more symmetrical map than the unrelaxed cluster, A2255. Here, we calculate an asymmetry factor of the smoothed map of member galaxies. First, the ‘total fluctuation power’ of the map within a radius of $r_{500} = 2/3 r_{200}$ is calculated as

$$S^2 = \sum_{i,j} I^2(x_i, y_j). \quad (5)$$

Then, we get the ‘difference power’ of the map for all symmetric pixels,

$$\Delta^2 = \sum_{i,j} [I(x_i, y_j) - I(-x_i, -y_j)]^2 / 2. \quad (6)$$

The asymmetry factor of a cluster, α , is defined as

$$\alpha = \frac{\Delta^2}{S^2}. \quad (7)$$

Here, $\alpha = 0$ implies a very symmetric morphology of a cluster, whereas $\alpha = 1$ indicates a highly asymmetric morphology.

3.3 Ridge flatness, β

Smoothed optical map (middle panels of Fig. 2) of a relaxed cluster generally has a steep surface brightness profile in all directions. Substructures appear in the smoothed map of an unrelaxed cluster, and there usually exists a ‘ridge’ extended from the cluster center to a certain direction in the smoothed map.

We first get light profiles in various directions. For a given direct ϕ (0° in the north, 90° in the east), we fit the light profile with a one-dimensional King model (King 1962)

$$I_{1D}(r) = \frac{I_0}{1 + (r/r_0)^2}, \quad (8)$$

where r is the cluster centric distance in the given direction, I_0 is

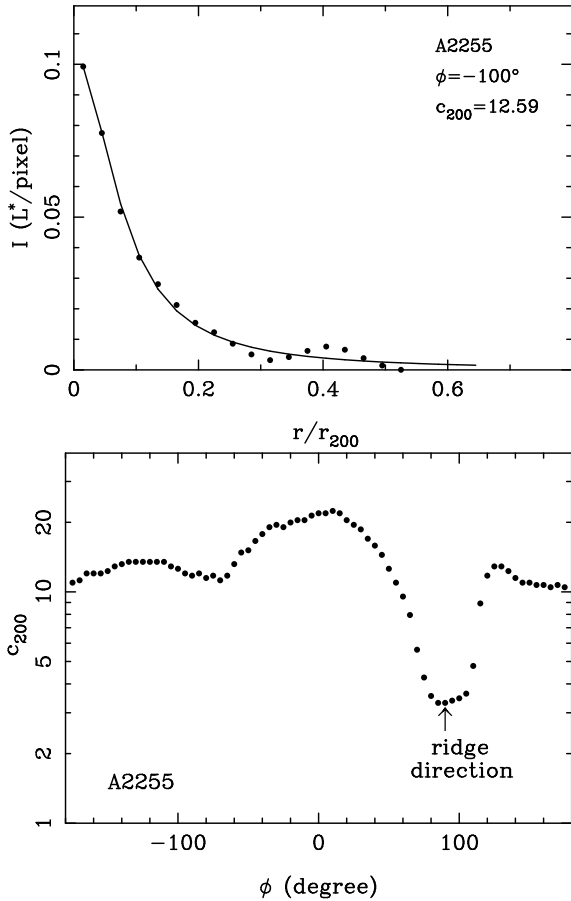


Figure 3. An example for relative ridge steepness factor. The upper panel shows the light profile at a direction and one-dimensional King model. The lower panel shows variations of steepness factors for all directions. The arrow indicates the ridge direction with the minimum steepness factor.

the luminosity density at cluster center and r_0 is characteristic radius of the one-dimensional King model. We now define the steepness factor as $c_{200} = r_{200}/r_0$. For each cluster, we calculate c_{200} in 72 direction (5° each section) and get the mean value of the steepness factor, $\langle c_{200} \rangle$.

The direction with the most flat profile is recognized as the ridge on the map, which very likely indicates the axis of cluster merging and has the minimum steepness factor, c_{200}^R . The ridge flatness is defined as the relative steepness of the ‘ridge’ to those of other directions,

$$\beta = \frac{c_{200}^R}{\langle c_{200} \rangle}. \quad (9)$$

For very relaxed clusters, the light profiles are similarly steep in all directions, so that $\beta \sim 1$. For unrelaxed clusters, a flatter ridge in the map gives a smaller β . For example, the profiles of A2255 have similar steepness of $c_{200} \sim 12$ in most directions (Fig. 3), but in the ridge direction a much small value of $c_{200}^R \sim 4$, and hence the cluster has a very small of $\beta \sim 0.33$.

3.4 Normalized deviation, δ

Relaxed clusters have very similarly smooth brightness profiles in all directions, so that the smoothed optical map can be fitted by, e.g., the two-dimensional elliptical King model. The unrelaxed

clusters have many substructures in the map, which result in more deviation of the smoothed optical map from the model.

First, we model the smoothed map of a cluster within the region of $r_{500} = 2/3 r_{200}$ with a two-dimensional elliptical King model of

$$I_{2D\text{model}}(x, y) = \frac{I_0}{1 + (r_{\text{iso}}/r_0)^2}, \quad (10)$$

where I_0 is the luminosity density at cluster center, r_0 is the characteristic radius of the two-dimensional King model, r_{iso} is the cluster centric ‘distance’ of an isophote,

$$r_{\text{iso}}^2 = [x \cos(\theta) + y \sin(\theta)]^2 + \epsilon^2[-x \sin(\theta) + y \cos(\theta)]^2, \quad (11)$$

where ϵ is the ratio of semiminor axis to semimajor axis of an isophote ($\epsilon \leq 1$), θ is the position angle of the major axis. The normalized deviation δ of the residual map after the model fitting is defined as

$$\delta = \frac{\sum_{i,j} [I(x_i, y_j) - I_{2D\text{model}}(x_i, y_j)]^2}{S^2}, \quad (12)$$

here S is defined in Equation 5. For a relaxed cluster, the smoothed map can be well fitted by a two-dimensional King model, so that the deviation δ is small. A large δ means a larger deviation from the best-fitting King model, which is an indication of substructures produced by, e.g., violent mergers (see right panels of Fig. 2).

3.5 Uncertainties of α , β and δ

The uncertainties of α , β and δ of a galaxy cluster mainly come from the contamination and incompleteness of member galaxies. For the cluster sample in Table 1, checking with available spectroscopic data, we find that the contamination rate and incompleteness for luminous member galaxies of $M_r^e(z) \leq -20.5$ within a radius of r_{500} are about 10%, 5%, respectively.

We apply Monte Carlo simulations to estimate the uncertainties. For each cluster, a fraction of recognized member galaxies are randomly selected and assumed to be contamination. After removing the contamination, we get a new partially removed member galaxy data. Considering the estimation of incompleteness on the uncertainties is the same as that of contamination, we randomly remove a small fraction (15%) of the recognized member galaxies (not the BCG anyway). Follow the calculations described above, we get values of α , β and δ for the partially removed dataset for 50 times. The scatter of the values is taken as the uncertainty.

3.6 Relaxation parameter, Γ , and optimization

Based on photometric data of a cluster, the α , β and δ values can be calculated with properly assumed σ_a and σ_b . All these three parameters are related to the dynamical state of a cluster, but they are not independent. We here seek the best combination of the three parameters, and define the relaxation parameter, Γ , for quantification of cluster dynamical state, which should be able to effectively separate the relaxed and unrelaxed states of the test clusters in Table 1.

First of all, for the smooth scale with a set of σ_a and σ_b , we obtain the smoothed maps of clusters in Table 1, and then calculate the quantities of α , β and δ . We find that a large smooth scale may erase the merging features for unrelaxed clusters, while a small scale may result in discrete patches in the smoothed map for misclassification. Therefore, the optimal values of σ_a and σ_b should be

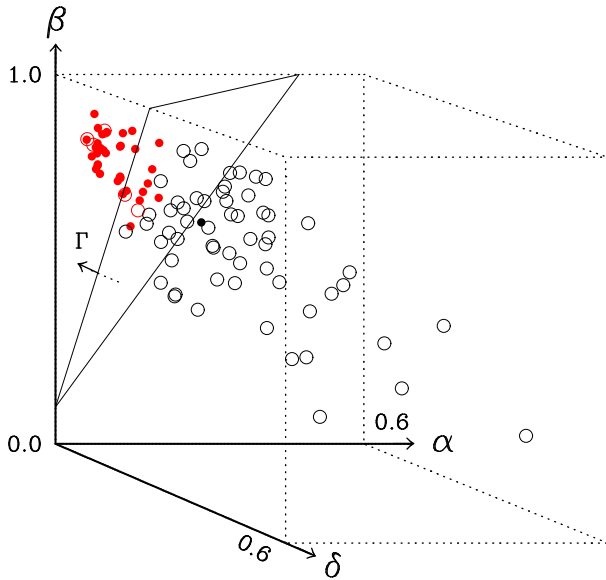


Figure 4. In the three-dimensional space of α , β and δ , relaxed clusters in Table 1 are shown by dots and unrelaxed clusters are shown by open circles. The α , β and δ values are calculated with smooth scale parameters of $\sigma_a = 0.03$, $\sigma_b = 0.15$. The plane outlined by thin solid lines can separate the relaxed and unrelaxed clusters. Clusters farther than the plane are shown in red color. The relaxation parameter Γ is defined as the distance to the plane.

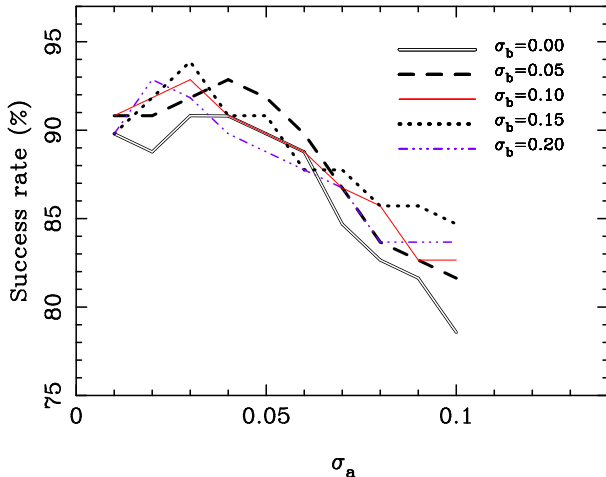


Figure 5. Success rate for the separation of the relaxed and unrelaxed clusters in Table 1 as a function of σ_a . Different curves are plotted for different σ_b .

sought to separate the relaxed and unrelaxed clusters in the three-dimensional space of α , β and δ (see Fig. 4) by a plane which we will define below.

Clearly, relaxed clusters in general have larger β values and smaller α and δ values than the unrelaxed clusters. The data distribution in the three-dimensional space of α , β and δ in Fig. 4 shows that the relaxed and unrelaxed clusters can be separated by a plane:

$$\beta = A\alpha + B\delta + C. \quad (13)$$

The optimal plane should give the maximum rate of successful separation. For any set of σ_a and σ_b , we find the optimal plane. After some iterations, we find that separation reaches the maximum

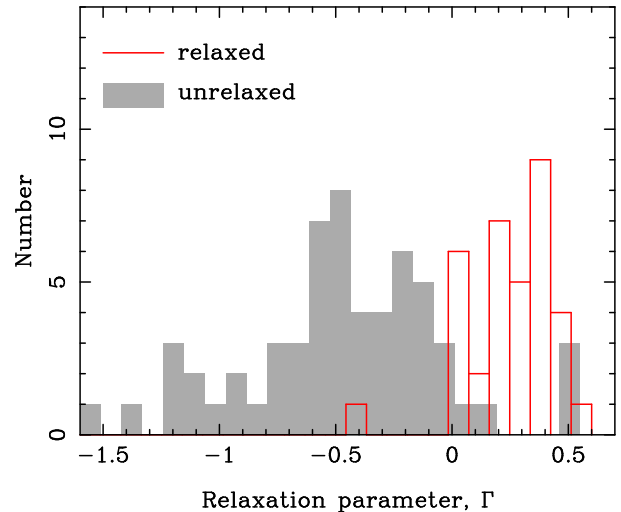


Figure 6. Histogram for relaxation parameters of relaxed and unrelaxed clusters in Table 1.

rate of 93.9% for the relaxed and unrelaxed clusters in Table 1 (see Fig. 5). The optimal value of σ_a is found to be 0.03 and that of σ_b is 0.15, the optimal plane has the parameters of $A = 1.9$, $B = 3.58$ and $C = 0.1$.

Now, we define the relaxation parameter, Γ , to quantify dynamical state of a cluster, which is the distance to the optimal plane (see Fig. 4):

$$\Gamma = [\beta - (1.90\alpha + 3.58\delta + 0.10)]/k, \quad (14)$$

here $k = \sqrt{1 + A^2 + B^2}$. In practical calculation, we ignore the constant factor k (i.e., $k = 1$). The relaxation parameter is positive for relaxed clusters and negative for unrelaxed clusters. A larger Γ means that a cluster appears more relaxed.

We have calculated the values for α , β , δ and Γ for clusters in Table 1. The relaxed and unrelaxed clusters are well separated in the three-dimensional space by the plane shown in Fig. 4, see also the histogram in Fig. 6. A few exceptions are discussed in Appendix. As shown by examples in Fig. 7, clusters with a low negative value of Γ have irregular distributions of member galaxies and no dominant central galaxies.

In some merging clusters, BCGs are not located in the cluster center (Wen et al. 2009; Einasto et al. 2012). Our calculations for the center on the BCGs give very low value of β and high values of α and δ , and then such clusters are recognized as unrelaxed with a very negative Γ .

3.7 Tolerance of the relaxation parameter on faint member galaxies and cluster radius

In definition of the relaxation parameter of a cluster, we have taken the luminosity threshold of member galaxies as an absolute magnitude of $M_r^e = -20.5$. Now we investigate the tolerance of the relaxation parameter by discarding the faint member galaxies and setting the threshold $M_r^e = -21.0$, so that α , δ , β and Γ values are calculated by using less member galaxies. For clusters in Table 1, we find that the Γ values are very consistent with each other for the two thresholds (the upper panel of Fig. 8), which suggests that the incompleteness of faint member galaxies does not affect the estimation of relaxation parameter, Γ , as long as there are enough luminous member galaxies used for calculations.

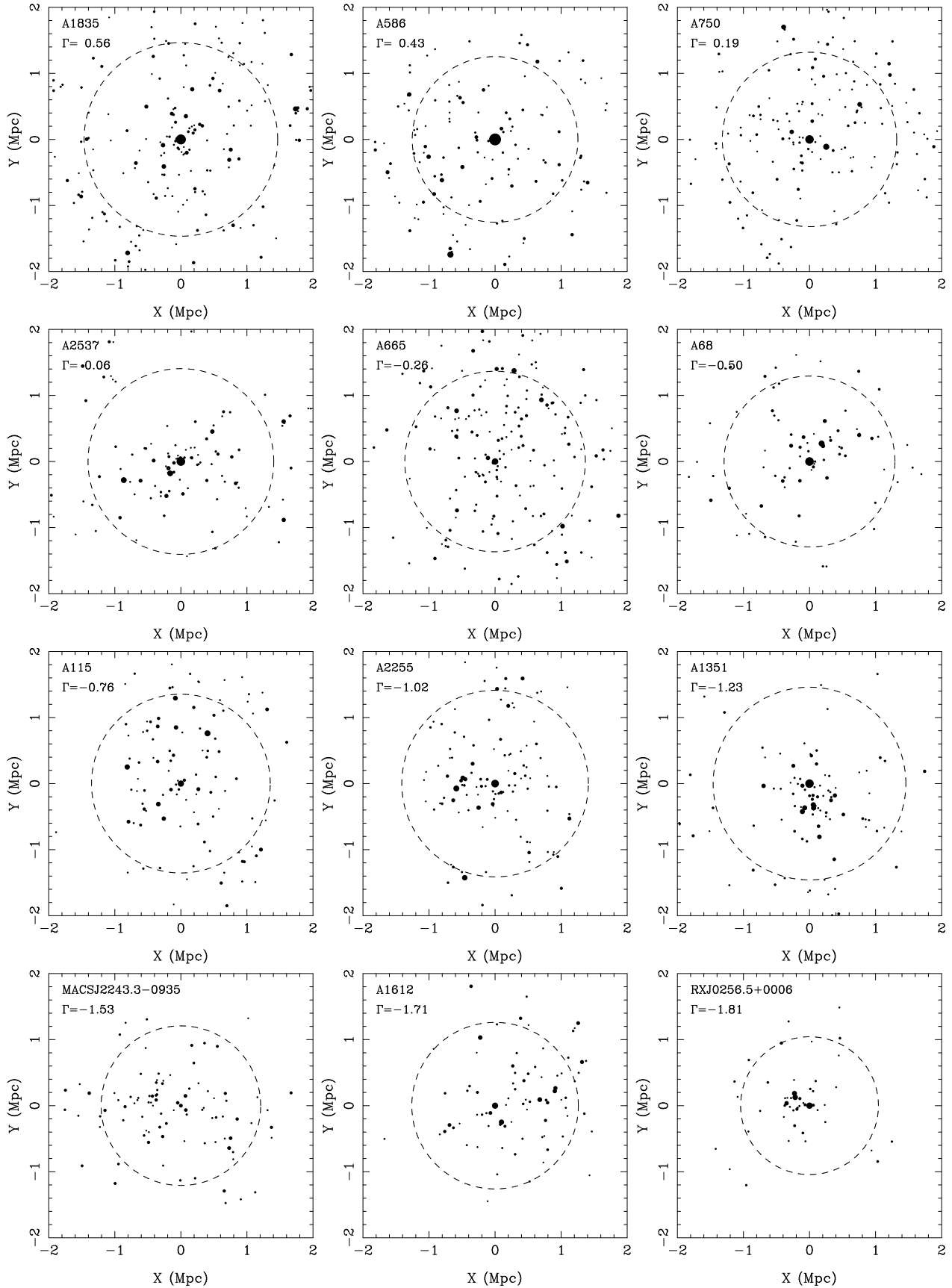


Figure 7. Distribution of cluster member galaxies of 12 example clusters with different Γ values in the range of $-2 \lesssim \Gamma < 0.6$. Sizes of black dots are scaled by the square root of galaxy luminosities. A large positive Γ indicates the relaxed state of clusters, and a very negative Γ indicate the very unrelaxed state. Large circles indicate the central region of clusters with a radius of r_{500} .

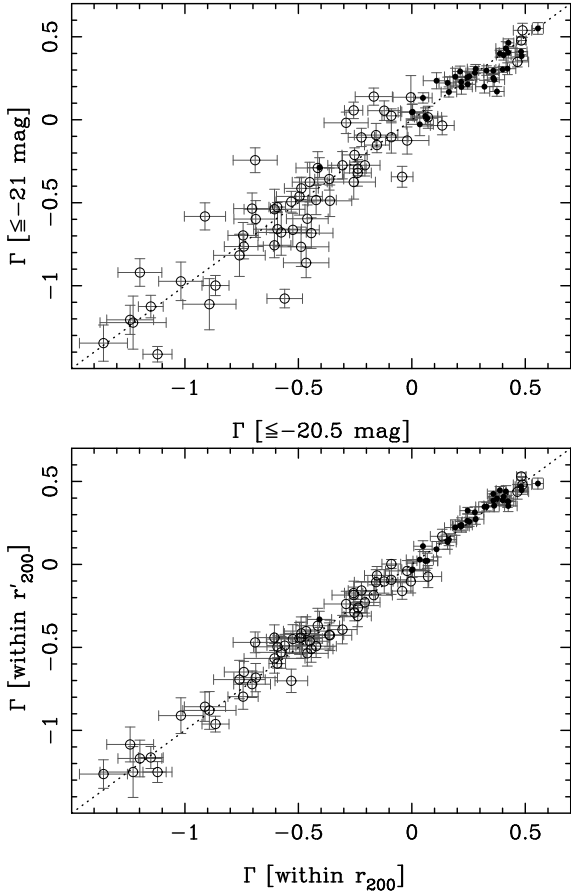


Figure 8. Comparison of relaxation parameters of clusters in Table 1 calculated with different thresholds for absolute magnitudes of member galaxies (upper panel) or different estimates for cluster radii (lower panel). Relaxed clusters are plotted as black dots and unrelaxed clusters as open circles.

The relaxation parameter, Γ , is derived from α , δ and β within the central region of an area of $r_{500} = 2/3r_{200}$. It is also possible that r_{200} has some uncertainty. We investigate the tolerance of relaxation parameters on the cluster radius, by assuming that r_{200} in Table 1 is systematically overestimated so that the real radius $r'_{200} = 0.9r_{200}$. With the assumed smaller cluster radii, some member galaxies in the outer region are discarded and the smooth scales also become systematically smaller than the original values according to Equation (4). We calculate α , δ and β and Γ , and find very good agreement between original and new Γ values (the lower panel of Fig. 8).

3.8 Comparison of Γ with dynamical state parameters estimated from X-ray data

Previously, substructures and dynamical states of clusters were often estimated from X-ray data, as represented by the concentration (e.g. Santos et al. 2008), the centroid shift (e.g. Mohr et al. 1995) and the power ratio (e.g. Buote & Tsai 1995) derived from X-ray image. Cooling time of hot gas derived from X-ray spectra sometimes was also used as indication of dynamical states (e.g. Voigt & Fabian 2004; Bauer et al. 2005). Now we compare the relaxation parameters with the dynamical parameters derived from X-ray data.

The first dataset of X-ray dynamical parameters are taken

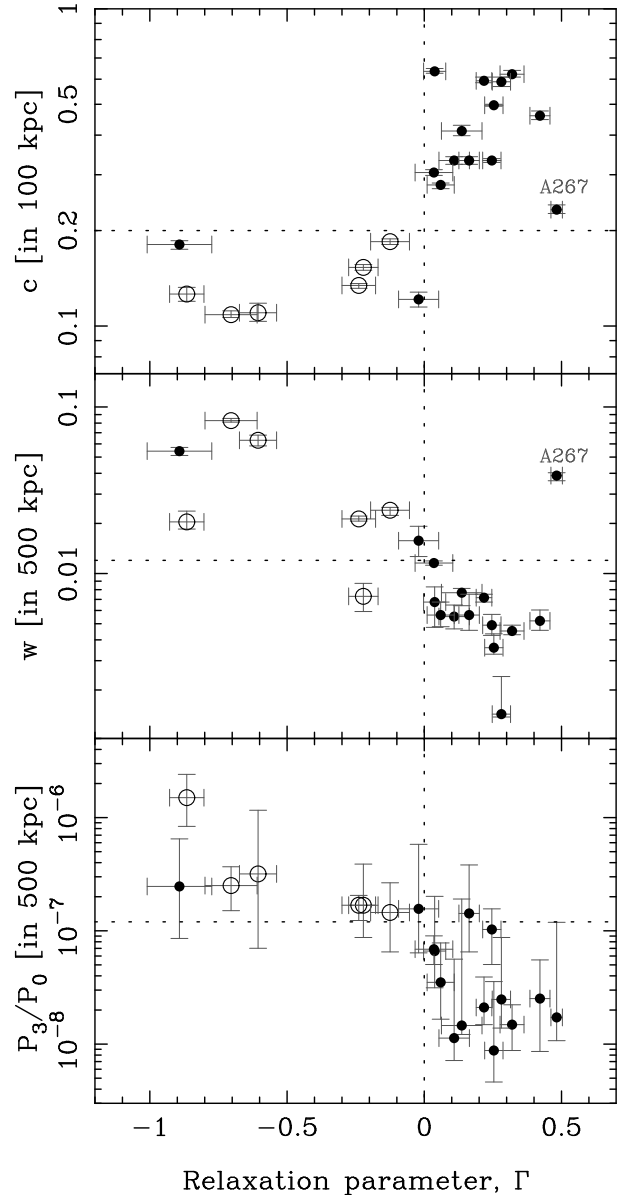


Figure 9. Correlation between the relaxation parameter, Γ , with the concentration c (upper panel), centroid shift w (middle panel) and the power ratio P_3/P_0 (lower panel) derived from X-ray data by Cassano et al. (2010) for 21 clusters. The black dots are clusters without radio halo detections, and open circles are clusters with radio halo detections. The horizontal dotted lines indicate the separation between radio halo and no-radio halo clusters by Cassano et al. (2010), the vertical line indicates the separation between relaxed and unrelaxed clusters by Γ .

from Cassano et al. (2010) who have the concentration, centroid shift and power ratio measurements of X-ray images published for 32 clusters. There are 21 clusters in the SDSS-III region (A267, A611, A697, A773, A781, A1423, A1682, A1758, A2219, A2261, A2390, A2537, A2631, MACS J1115.8+0129, MACS J2228.5+2036, RXC J0437.1+0043, RXC J1504.1-0248, RX J1532.9+3021, Z2089, Z2701, Z7160), 19 of which have been listed in Table 1. We also calculate the relaxation parameters for the other two clusters (RXCJ0437.1+0043, Z2089). In this sample of 21 clusters, six of them have radio halos detected and are most probably merging clusters, and other 15 have not. Comparisons of

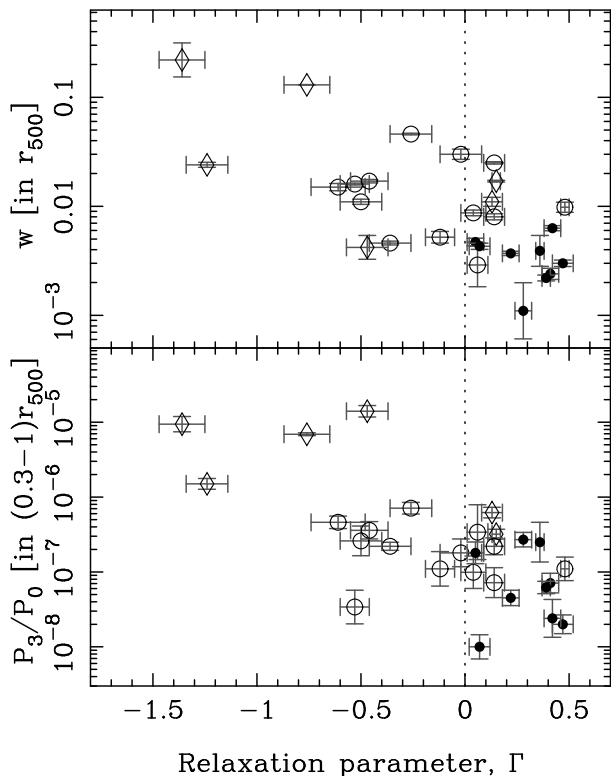


Figure 10. Similar to Fig. 9 but for the dynamical parameters (w and P_3/P_0) of 28 X-ray clusters derived by Weißmann et al. (2013), who have visually classified the clusters into ‘regular’ (black dots), ‘intermediate’ (open circle), ‘double’ and ‘complex’ (diamond) morphology categories.

the relaxation parameter, Γ , with the concentration c , centroid shift w and power ratio P_3/P_0 are shown in Fig. 9. The correlations are reasonable except for A267. The clusters with and without radio halos can be well separated.

The second dataset of X-ray dynamical parameters are taken from Weißmann et al. (2013). In their sample, there are 28 rich clusters in the area of the SDSS-III with an optical richness of $R_{L*} \geq 50$ (A13, A68, A115, A267, A383, A665, A773, A963, A1413, A1589, A1689, A1763, A1775, A1914, A2065, A2626, A2390, A2537, A2631, RXC J0003.8+0203, RXC J0821.8+0112, RXC J1302.8–0230, RXC J1516.3+0005, RXC J1516.5–0056, RXC J2157.4–0747, RXC J2129.6+0006, Z3146, Z7160), among which 25 clusters are in Table 1. We get the relaxation parameters Γ for other three clusters (A1775, RXCJ1302.8–0230, RXCJ1516.3+0005). Reasonable correlations between our relaxation parameters with dynamical parameters (w and P_3/P_0) are shown in Fig. 10.

Previous studies show that relaxed clusters have shorter cooling time than unrelaxed clusters (e.g. Fabian 1994; Voigt & Fabian 2004; Bauer et al. 2005; Peterson & Fabian 2006). The cooling times of 28 clusters in the SDSS-III region (A68, A115, A267, A586, A665, A697, A750, A773, A781, A963, A1423, A1682, A1758, A1763, A1835, A1914, A2111, A2219, A2259, A2261, A2390, RX J1532.9+3021, RX J1720.1+2638, RX J2129.6+0006, Z1953, Z2701, Z3146, Z7160) have been derived from X-ray data by Bauer et al. (2005). All these clusters are included in Table 1. Fig. 11 shows that the relaxation parameter Γ and cooling time t_{cool} at a radius of 50 kpc are well correlated. Almost all clusters with cool cores of $t_{\text{cool}} \leq 10$ Gyr have $\Gamma > 0$.

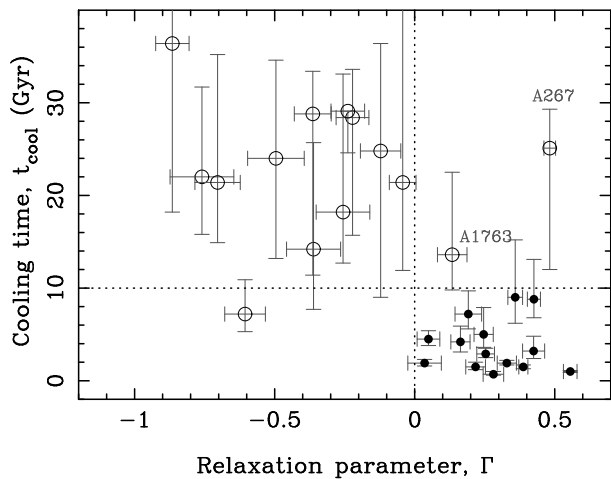


Figure 11. Comparison between the relaxation parameter, Γ , and cooling time at a radius of 50 kpc for 28 clusters derived from X-ray data (Bauer et al. 2005). The black dots and open circles indicate relaxed and unrelaxed clusters, respectively. The horizontal and vertical dotted lines indicate $\Gamma = 0$ and $t_{\text{cool}} = 10$ Gyr.

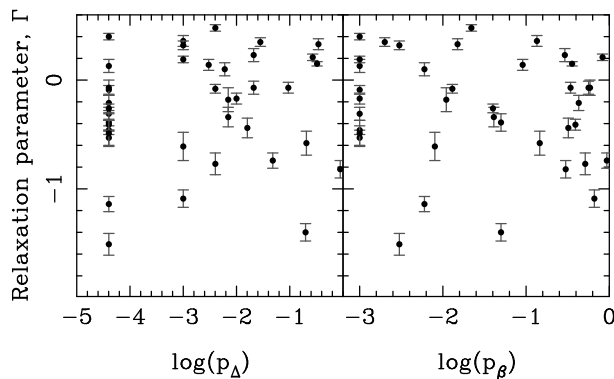


Figure 12. Comparison between the relaxation parameter, Γ , with the substructure significances by three-dimensional Dressler-Shectman test (left panel) and two-dimensional β (i.e., asymmetry) test derived by Einasto et al. (2012).

3.9 Comparison of Γ with previous optical study of substructures

Based on the SDSS spectroscopic data, Einasto et al. (2012) searched for substructures in 109 rich clusters of Tempel et al. (2012) by using a number of one-, two- and three-dimensional tests. Their three-dimensional tests include the Dressler-Shectman test (Dressler & Shectman 1988) and the α test which measures the centroid shift of cluster galaxies weighted by local velocity dispersion (West & Bothun 1990). Their two-dimensional test includes the β test which measures the asymmetry of galaxy distribution (West et al. 1988). These tests give p -values to quantify substructure significances. Smaller p -value means larger probability of substructure. Among the Einasto et al. (2012) sample, 13 clusters (A1589, A1650, A1750, A1795, A1904, A1991, A2029, A2048, A2061, A2065, A2069, A2142, A2244) are included in our Table 1 and 26 clusters (A628, A671, A933, A1066, A1205, A1307, A1516, A1541, A1552, A1569, A1663, A1691, A1767, A1775, A1809, A1831, A1913, A1999, A2020, A2022, A2079, A2124,

Table 2. Relaxation parameters of 2092 rich clusters in the SDSS (see online Supporting Information for the full table).

Name	R.A. (deg)	Dec. (deg)	z	flag $_z$	r_{BCG}	r_{200} (Mpc)	R_{L*}	N_{200}	Γ	σ_{Γ}
(1)	(2)	(3)	(4)	(5)	(6)	(7)	(8)	(9)	(10)	(11)
WHL J000012.6+103806	0.05238	10.63509	0.1824	0	16.70	1.43	56.77	38	-1.67	0.10
WHL J000021.7+150612	0.09053	15.10328	0.2991	0	17.72	1.47	54.05	38	-0.09	0.06
WHL J000026.3+215405	0.10958	21.90143	0.1665	0	16.17	1.52	57.68	39	-0.30	0.08
WHL J000039.9+300305	0.16637	30.05137	0.1906	0	16.51	1.48	54.85	39	-0.15	0.06
WHL J000111.5+213213	0.29792	21.53696	0.4000	0	18.75	1.53	68.03	55	-1.06	0.11
WHL J000117.2-031648	0.32183	-3.28003	0.2974	0	17.74	1.43	57.24	37	-0.72	0.14
WHL J000126.3-000143	0.35969	-0.02867	0.2465	1	16.93	1.46	58.61	34	-0.33	0.06
WHL J000158.5+120358	0.49367	12.06612	0.2086	0	15.91	1.75	88.28	65	0.55	0.04
WHL J000311.6-060530	0.79826	-6.09169	0.2484	0	16.72	1.79	115.74	88	-0.69	0.06
WHL J000318.1+043739	0.82531	4.62755	0.0989	0	14.18	1.37	64.51	32	0.52	0.03

Note. Column (1): cluster name with J2000 coordinates of cluster. Column (2): R.A. (J2000) of BCG. Column (3): Dec. (J2000) of BCG. Column (4): redshift. It is spectroscopic redshift if the flag in Column (5) is ‘1’, or photometric redshift if the flag is ‘0’. Column (5): flag of redshift. Column (6): r -band magnitude of BCG. Column (7): r_{200} of cluster (Mpc). Column (8): cluster richness. Column (9): number of member galaxies within r_{200} . Column (10) and (11): relaxation parameter and uncertainty.

A2175, A2245, A2249, J141735.5+020312) in our Table 2 (Section 4.1).

Fig. 12 shows the comparison between the relaxation parameter, Γ , with the substructure significances estimated by three-dimensional Dressler-Shectman test and two-dimensional β test for the 39 clusters in Einasto et al. (2012). We do not find significant correlations, which is somehow unexpected. Our calculations are based on the smoothed map of member galaxy distribution weighting their luminosities. The relaxation parameter we derive reflects the substructure of brightness distribution of member galaxies within the radius r_{500} , so that it has good correlations with dynamical state parameters from X-ray data (see Section 3.8). We notice that the cluster sizes Einasto et al. (2012) work on are a few ($\sim 5-7$) times of cluster virial radii for above 39 clusters (Tempel et al. 2012). The substructure significances they estimated may reflect the global substructures for position and velocity distributions of member galaxies within a much larger region than r_{500} .

4 DYNAMICAL STATES OF 2092 RICH CLUSTERS

Compared to the dynamical parameters derived from X-ray data for clusters, the relaxation parameter we defined has the advantage that it can be easily estimated from optical photometric data for positions and optical magnitude of member galaxies. It has successfully separated the known relaxed and unrelaxed clusters of the test sample of rich clusters with a rate of 94%. We can apply the method to all rich clusters to diagnose their dynamical state of clusters whenever the optical photometric data for member galaxies are available.

Wen et al. (2012) have identified 132 684 clusters in the redshift range of $0.05 < z < 0.8$ from the SDSS-III. Using photometric redshifts of galaxies, we recognized a cluster when the richness $R_{L*} \geq 12$ and the number of member galaxies $N_{200} \geq 8$ within a photometric redshift slice of $z \pm 0.04(1+z)$ and a radius of r_{200} . In this work, the spectroscopic redshifts of clusters are adopted if available, otherwise photometric redshifts are used. We have used the spectroscopic data of the SDSS DR9 (Ahn et al. 2012) to update member galaxy list, r_{200} and richness estimates for galaxy clusters taken from the catalog of Wen et al. (2012). Galaxies are removed from the member galaxy list if they have a velocity dif-

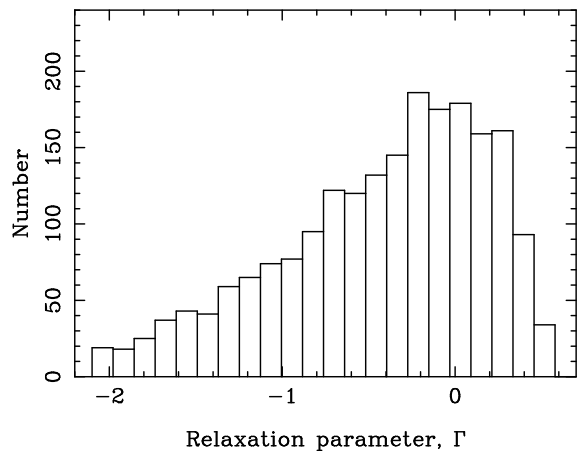


Figure 13. Histogram distribution of relaxation parameters for 2092 rich clusters.

ference $\Delta v > 2500 \text{ km s}^{-1}$ from cluster redshift and the missing galaxies in the photo- z data are included if they have a velocity difference $\Delta v \leq 2500 \text{ km s}^{-1}$ from cluster redshift. The cluster richness, R_{L*} , and radius, r_{200} , are then recalculated.

In this section, we quantify the dynamical states for 2092 rich clusters (Table 2) in the redshift range of $0.05 < z \leq 0.42$ with a richness of $R_{L*} \geq 50$. The redshift range is selected to make the cluster sample and the member galaxies approximately volume-limited complete (Wen et al. 2012). Above the richness, the reliability of cluster identification is nearly 100%.

4.1 Distribution of relaxation parameters, Γ

The relaxation parameters Γ of these 2092 rich clusters are calculated from α , β and δ by using the smoothed photometric data of the SDSS. Fig. 13 shows the histogram distribution of relaxation parameters for 2092 rich clusters. The values of Γ have a continuous distribution in the range of $-2.0 \lesssim \Gamma < 0.6$ with a peak at $\Gamma \sim 0$, which indicates that most clusters have intermediate dynamical states, rather than clearly very relaxed or very unrelaxed.

If the relaxed clusters are defined as those having $\Gamma \geq 0$, 28.2% (589) of 2092 clusters are relaxed. A few clusters with a non-

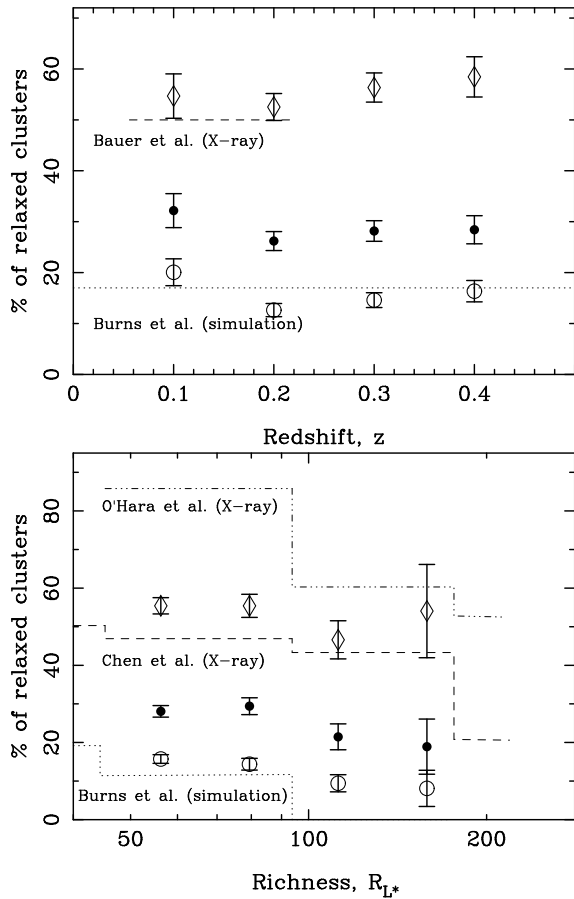


Figure 14. Fraction of relaxed clusters does not vary with redshift (upper panel) and richness (lower panel). The black dots are the fractions of relaxed clusters defined by $\Gamma \geq 0$, open circles for $\Gamma \geq 0.2$ and diamonds for $\Gamma \geq -0.4$. In the upper panel, result from previous simulation by Burns et al. (2008) is shown by the dotted line. The result from X-ray data by Bauer et al. (2005) is shown by the dashed line. In the lower panel, previous result from simulations by Burns et al. (2008) is shown by the dotted line, and result from the X-ray data in O’Hara et al. (2006) by dash-dotted line and that from X-ray data in Chen et al. (2007) by the dashed line.

Gaussian velocity distribution experience ongoing merger exactly along the line of sight (Einasto et al. 2012; Ribeiro et al. 2013) and can not be recognized by our two-dimensional method (see Appendix). This fraction of relaxed clusters should be taken as an upper limit. The fraction of relaxed clusters does not significantly vary with redshift and richness (Fig. 14), which is also found if the criterion for relaxed clusters is changed to be $\Gamma \geq 0.2$ or $\Gamma \geq -0.4$.

This constant fraction is very consistent to the result for a complete X-ray sample of 108 clusters in $0.15 < z < 0.7$, from which Mann & Ebeling (2012) found that 27 X-ray-luminous clusters are merger and that the merger fraction does change at $z < 0.4$ but starts to increase with redshift at $z \sim 0.4$. As clusters with cool cores are mostly relaxed clusters, Bauer et al. (2005) showed that the fraction of X-ray cool-core clusters do not vary with redshift at $z < 0.2$. Our result of no redshift dependence of relaxation parameters is consistent with the conclusion of Bauer et al. (2005) and also numerical simulations of Burns et al. (2008). The fractions of cool-core clusters were claimed to vary with cluster mass from X-ray data (O’Hara et al. 2006; Chen et al. 2007; Burns et al. 2008). Using optical spectroscopic data, Einasto et al. (2012) found that richer clusters tend to have more substructures. However, our re-

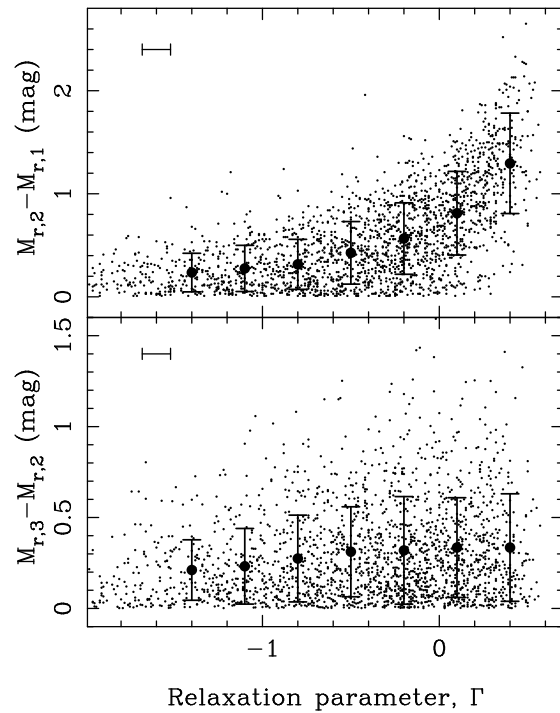


Figure 15. Magnitude difference between the first BCG and second BCG (upper panel) and between the second BCG and third BCG (lower panel) against the relaxation parameter for 2092 rich clusters. The uncertainty of magnitude difference is less than 0.05 mag, and the typical error-bar of Γ is shown on the top left. The average and data scatter in seven bins are plotted to show the dependence.

sults show almost no obvious richness dependence for the fraction of relaxed clusters within $R_{L*} \geq 50$ (see lower panel of Fig. 14). This inconsistency needs to be investigated in future.

Our optical cluster sample is approximately volume-limited complete, while the X-ray clusters are usually flux limited or flux selected. Clusters with cool cores are more likely to be detected and selected in X-ray because they have high X-ray peaks in the central region (Hudson et al. 2010). As shown by the simulations of Eckert et al. (2011), the flux-limited X-ray cluster samples are significantly biased for clusters with cool cores. This selection effect is more serious at lower redshift and lower mass, which may explain the higher fraction ($\sim 50\%$) of cool-core clusters for flux-limited X-ray sample (e.g., Chen et al. 2007) than the fraction (28%) of relaxed clusters in our optical sample.

To verify the selection effect of X-ray sample, we cross-match the 2092 clusters with the X-ray selected clusters in the *ROSAT* all sky survey (Böhringer et al. 2000a, 2004), and get 159 matches. Among this X-ray detected subsample, 74 clusters (46.5%) have $\Gamma \geq 0$. This fraction is very close to the fraction of cool-core clusters (Bauer et al. 2005; Chen et al. 2007) but significantly larger than 28.2% for our sample in Table 2.

4.2 Relaxation parameter and BCG dominance

Very relaxed clusters in general have one very luminous BCG, and unrelaxed clusters usually have more than one similarly brightest member galaxies (see Fig. 7). We now check if the BCG dominance is related to cluster dynamical state quantified by the relaxation parameter.

The BCG dominance is best shown by the difference of abso-

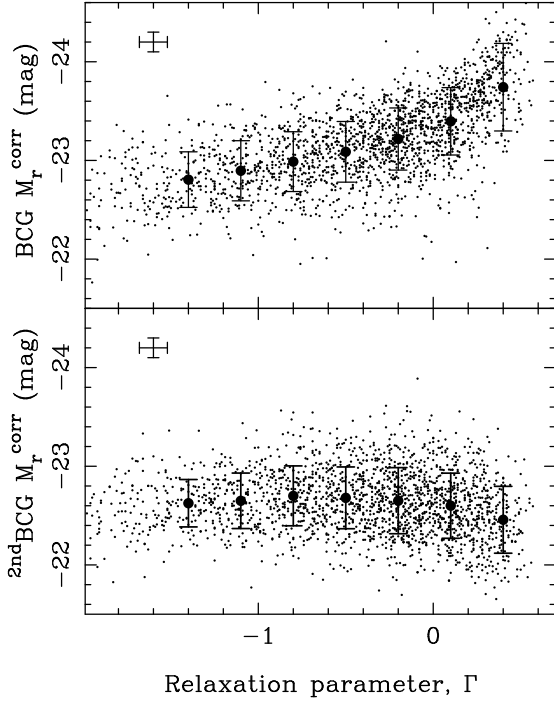


Figure 16. Absolute magnitude of the first BCG (upper panel) and second BCG (lower panel) in the r band, after the redshift evolution and richness dependence (Wen et al. 2012) being diminished, against relaxation parameter. The cross bar on the top left indicates typical errors. The average and data scatter of the magnitudes in seven bins are plotted to show the dependence.

lute magnitudes of the first and second BCGs, e.g., $M_{r,2} - M_{r,1}$, in the r band. As shown in the upper panel of Fig. 15, the magnitude difference obviously tends to be larger for clusters with a larger relaxation parameter, which indicates that the BCG dominance is closely related to dynamical states of clusters (Ramella et al. 2007; Smith et al. 2010). However, the magnitude difference between the second and third BCGs, $M_{r,3} - M_{r,2}$, does not show significant dependence on relaxation parameter (the lower panel of Fig. 15).

We further check if more relaxed clusters have an absolutely more luminous BCG, in addition to the relative BCG dominance. Wen et al. (2012) noticed that BCG absolute magnitudes, after k -correction, evolves with redshift and depends on richness. These effects have to be diminished to show the dependence of absolute magnitude on dynamical state. We correct these effects according to equations 7 and 9 in Wen et al. (2012), so that the corrected r -band absolute magnitude is defined as

$$M_r^{\text{corr}} = M_r + 1.50z + 1.10 \log(R_{L^*}/50). \quad (15)$$

As shown in the upper panel of Fig. 16, the corrected BCG absolute magnitude is related to the dynamical state. More relaxed clusters host a more luminous first BCG (Smith et al. 2010). The corrected absolute magnitude of the second BCG is not obviously related to the dynamical state (the lower panel of Fig. 16).

We now conclude that BCG absolute magnitude and its relative dominance are related to cluster dynamical state, in addition to the known redshift evolution and dependence of cluster richness.

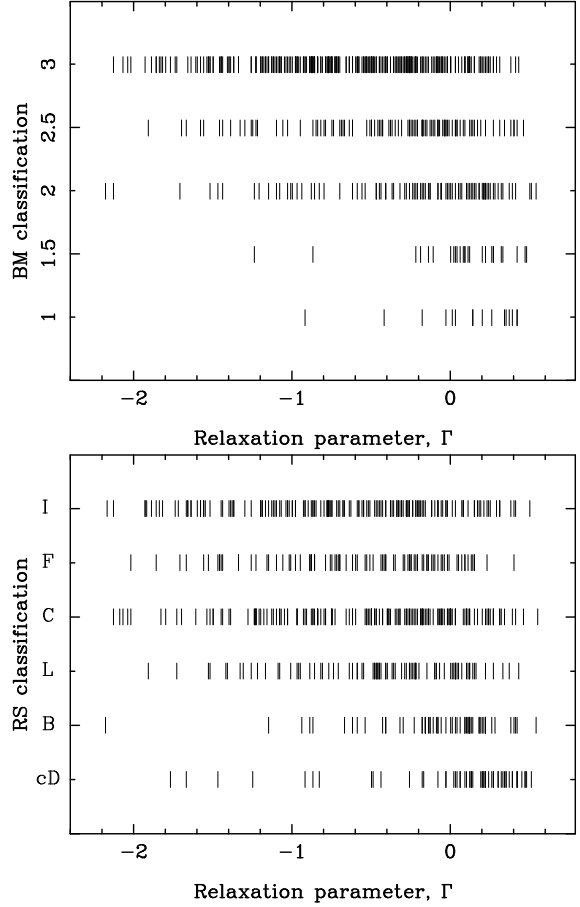


Figure 17. Relaxation parameters for clusters with different BM cluster classification (Bautz & Morgan 1970, upper panel) and with RS classification (Rood & Sastry 1971, lower panel).

4.3 Clusters classification and relaxation parameter

Galaxy clusters have been classified according to galaxy distribution in optical images (see Table 1 of Bahcall 1977, for details). The relaxation parameters we defined in this paper are derived from the luminosity distribution of member galaxies. It is expected that clusters of different types have different relaxation parameters.

Clusters are classified by Bautz & Morgan (1970, hereafter BM) for five types: I, I-II, II, II-III and III, based on the relative contrast of the BCG. Type I clusters contain a central cD galaxy, Type II clusters have a central galaxy between cD and Virgo-type giant ellipticals and Type III clusters have no dominant galaxies. Type I-II and Type II-III are the intermediate types between I and II and between II and III. Rood & Sastry (1971) classified clusters into six types: cD, B, L, C, F and I, based on the distribution of 10 brightest cluster member galaxies. The cD-type clusters contain an outstandingly cD galaxy, B-type clusters have two supergiant galaxies with a small separation, L-type clusters have three or more supergiant galaxies among the top 10 brightest galaxies with comparable separation in a line, C-type clusters have four or more brightest galaxies among the top 10 with comparable separations in the core, F-type clusters have several galaxies among the top 10 distributed in a flattened configuration, and I-type clusters have the top 10 brightest galaxies distributed irregularly.

We cross-match clusters in Table 2 with the Abell clusters (Abell et al. 1989) which have BM classification. Within a separa-

tion of r_{200} and a redshift difference of 0.05, we get 509 matches. Among them, 16, 28, 91, 102 and 272 clusters are of type I, I-II, II, II-III and III, respectively. In the upper panel of Fig. 17, we show the Γ distributions for the five BM types clusters. About 75% of type I and 79% of type I-II clusters have $\Gamma \geq 0$, while this fraction decreases to 40% for type II, 24% for type II-III and 14% for type III clusters. The Γ distributions also suggest that the type I and I-II clusters are more relaxed, while type II to type III tend to be more unrelaxed, consistent with the conclusion of Bahcall (1977).

There are 620 of 2092 clusters in Table 2 which have RS classifications in Struble & Rood (1987). Among them, 58, 60, 85, 165, 91 and 161 clusters are classified as cD, B, L, C, F and I types, respectively. The Γ distributions for these types are plotted in the lower panel of Fig. 17. The fractions of clusters with $\Gamma \geq 0$ for the cD and B type clusters (72% and 52%, respectively) are significantly larger than those for the L, C, F and I types (25%, 22%, 14% and 14%, respectively). The Γ distributions suggest that cD- and B-type clusters tend to be more relaxed, while F- and I-type clusters tend to be more unrelaxed.

4.4 Dynamical state and radio halo

Radio halos are diffuse radio emission in clusters not associated with any given member galaxies. Brunetti et al. (2009) found that for clusters with detected radio halo, the radio power of halos is closely related to the X-ray luminosity, by

$$\log(P_{1.4\text{GHz}}) - Y = A + b[\log(L_X) - X], \quad (16)$$

where $P_{1.4\text{GHz}}$ is the radio power at 1.4 GHz in unites of W/Hz, L_X is X-ray luminosity between 0.1 and 2.4 keV in unites of erg s^{-1} , $Y = 24.5$, $X = 45$, $A = 0.195 \pm 0.060$ and $b = 2.06 \pm 0.20$. However, low-frequency search for radio halos for some X-ray luminous clusters failed to detect radio halos (Venturi et al. 2008). The non-detection suggests the bimodality for the relation between X-ray luminosity and radio power (Brunetti et al. 2009). On the other hand, radio halos are exclusively detected from merging clusters (Buote 2001; Cassano et al. 2010), but there is no quantitative relation between radio power and the degree of the cluster disturbance. The information of cluster merger is expected to account for the scatter and the bimodality of the $P_{1.4\text{GHz}}-L_X$ relation. Here, we quantitatively investigate the correlation between the deviation of radio power from the $P_{1.4\text{GHz}}-L_X$ relation with the relaxation parameter.

We get the data for radio halo powers and X-ray luminosities of 15 clusters from Feretti et al. (2012): A665, A697, A746, A773, A781, A851, A1351, A1689, A1758, A1914, A1995, A2034, A2219, A2255 and A2256. All these clusters are listed in our Table 1. We get data for six clusters with mini halos, A1835, A2029, A2142 and RX J1504.1-0248 from Feretti et al. (2012) and A2390 and Z7160 from Brunetti et al. (2009), because the mini-halos also follow the same X-ray and radio relation. In addition, we include data of 16 X-ray luminous clusters of $R_{L*} \geq 50$ which have only the upper limits of radio halo powers because of non-detection of radio halos. The data are obtained for 12 clusters: A611, A1423, A2537, A2631, A2697, MACS J1115.8+0129, MACS J2228.5+2036, RX J0027.6+2616, RX J1532.9+3021, Z2701, Z5699 and Z7215 from Brunetti et al. (2009) and for four clusters: A267, A1576, A2261 and RXC J0437.1+0043 from Kale et al. (2013). All these clusters have been included in Table 2.

With the relation between X-ray luminosity and radio halo power, as shown in Equation 16, the radio halo powers of clus-

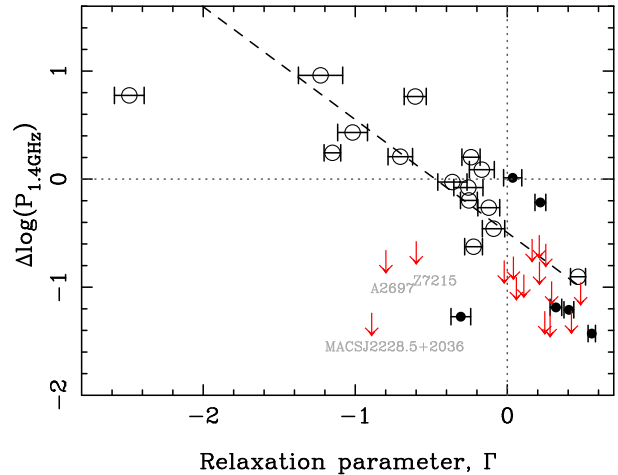


Figure 18. Deviation of radio halo power from the X-ray and radio relation is very closely related to the relaxation parameter, Γ . Radio power and X-ray luminosity are taken from by Feretti et al. (2012) and Brunetti et al. (2009) for radio halo clusters (open circles) and mini-halo clusters (black dots). The arrows are the upper limits of radio halo detection. The dashed line indicates the best fit.

ters can be predicated from the observed L_X . The deviations of the observed radio powers, $\Delta \log(P_{1.4\text{GHz}})$, from the predictions are then plotted against the relaxation parameter, Γ , in Fig. 18. We find a good correlation between the deviations and relaxation parameter, given by

$$\Delta \log(P_{1.4\text{GHz}}) = (-0.49 \pm 0.11) - (1.05 \pm 0.19) \Gamma, \quad (17)$$

for both the halos and mini-halos. Most X-ray luminous clusters with non-detection of radio halos are relaxed clusters. Their upper limits of radio powers are very close to the correlation line, except three outliers (A2697 with $\Gamma = -0.80 \pm 0.08$, MACS J2228.5+2036 with $\Gamma = -0.90 \pm 0.11$ and Z7215 with $\Gamma = -0.60 \pm 0.11$). Our result suggests that dynamical states of clusters are the main reason for the data scatter around the $P_{1.4\text{GHz}}-L_X$ relation in Fig. 8 of Feretti et al. (2012). This is the first time of quantitative demonstration that radio halo is not only related to X-ray luminosity but also to the dynamical state of clusters.

4.5 Dynamical state and X-ray luminosity

X-ray luminosities of clusters are tightly correlated with cluster masses (Chen et al. 2007). A good proxy of cluster masses is cluster richness defined as $R_{L*} = L_{200}/L^*$ in Wen et al. (2012) (also see Section 2.2). The correlation between cluster richness and X-ray luminosity given by Wen et al. (2012) is

$$\log(L_X) - 44.0 = -2.49 + 1.59 \log(R_{L*}). \quad (18)$$

The data have fairly scatter around this relation (see fig. 17 of Wen et al. 2012), but the reason is not clear. Popesso et al. (2007) showed that clusters in ongoing-merging process have a low X-ray luminosity, which implies that the dynamical states of clusters could influence the X-ray luminosity. Their study suggests that cluster dynamical state may account for the scatter of the L_X-R_{L*} relation. Here, we check if the deviation of X-ray luminosity from the L_X-R_{L*} relation is related to the relaxation parameter.

In our Table 2, 159 clusters have been detected in the ROSAT X-ray all sky survey (Böhringer et al. 2000a, 2004). Now, we assume that cluster masses, and hence cluster richnesses, are funda-

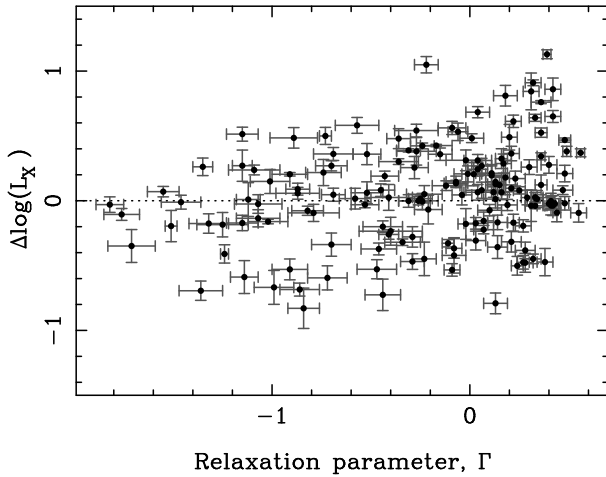


Figure 19. For 159 X-ray clusters in our sample detected by the *ROSAT* all sky survey, the deviations of X-ray luminosity from the richness– L_X relation given by Wen et al. (2012) are not correlated with the relaxation parameter, Γ . The dotted line indicates $\Delta \log(L_X) = 0$.

mentally related to cluster X-ray luminosity. Therefore, we can predict an X-ray luminosity from the richness by using Equation (18), and then get the offset between the predicted and observed X-ray luminosity, $\Delta \log(L_X)$. As shown in Fig. 19, we find very weak correlation between $\Delta \log(L_X)$ and Γ , which suggests that the global X-ray luminosity is insensitive to cluster dynamical state.

5 CONCLUSIONS

We presented a robust method to diagnose substructures and dynamical states of galaxy clusters by using the optical photometric data of member galaxy distribution. The distribution of member galaxies is smoothed by using a Gaussian kernel and a weight of their luminosities. The asymmetry factor, α , the ridge flatness, β , and the normalized deviation, δ , are then calculated from the smoothed map, based on which a relaxation parameter, Γ , is defined to quantify dynamical states of clusters. The smooth-scale and parameter combination are then optimized by using a test sample of 98 clusters with known dynamical states previously classified as relaxed and unrelaxed based on X-ray, optical and radio data. The newly defined relaxation parameter, Γ , can be used to distinguish the known relaxed and unrelaxed clusters with a success rate of 94%, only a few exception of mergers along the line of sight.

We calculated relaxation parameters for 2092 clusters in Wen et al. (2012) with a richness of $R_{L^*} \geq 50$ identified from SDSS. We found that the relaxation parameters are continuously distributed in a range of $-2 \lesssim \Gamma < 0.6$. Only 28% of 2092 rich clusters are classified as relaxed clusters with $\Gamma \geq 0$. This fraction is smaller than that of the matched X-ray subsample detected by the *ROSAT*, which confirms that the flux-selected X-ray cluster sample usually has a selection bias in dynamical state. The fraction of relaxed clusters does not vary significantly with redshift at $z \leq 0.42$ and with richness in the range of $R_{L^*} \geq 50$ (i.e., $M_{200} \geq 3.15 \times 10^{14} M_\odot$). Our results imply that a large fraction of clusters are still continuously growing even for massive ones. We found that the relaxation parameter strongly correlates with the absolute magnitude of BCGs and with the magnitude difference between the first and second BCGs, which indicates that BCG growth is related to dynamical state of its host cluster. For the first time,

we quantitatively showed that the emission power of radio halo not only depends on the X-ray luminosity but also the dynamical state of a cluster.

ACKNOWLEDGEMENTS

The authors are supported by the National Natural Science Foundation of China (10833003 and 11103032) and the Young Researcher Grant of National Astronomical Observatories, Chinese Academy of Sciences. Funding for SDSS-III has been provided by the Alfred P. Sloan Foundation, the Participating Institutions, the National Science Foundation and the US Department of Energy. The SDSS-III web site is <http://www.sdss3.org/>. SDSS-III is managed by the Astrophysical Research Consortium for the Participating Institutions of the SDSS-III Collaboration including the University of Arizona, the Brazilian Participation Group, Brookhaven National Laboratory, University of Cambridge, University of Florida, the French Participation Group, the German Participation Group, the Instituto de Astrofísica de Canarias, the Michigan State/Notre Dame/JINA Participation Group, Johns Hopkins University, Lawrence Berkeley National Laboratory, Max Planck Institute for Astrophysics, New Mexico State University, New York University, Ohio State University, Pennsylvania State University, University of Portsmouth, Princeton University, the Spanish Participation Group, University of Tokyo, University of Utah, Vanderbilt University, University of Virginia, University of Washington, and Yale University.

REFERENCES

- Abell G. O., Corwin Jr. H. G., Olowin R. P., 1989, *ApJS*, 70, 1
- Aguerri J. A. L., Sánchez-Janssen R., 2010, *A&A*, 521, A28
- Ahn C. P., et al., 2012, *ApJS*, 203, 21
- Aihara H., et al., 2011, *ApJS*, 193, 29
- Akamatsu H., Kawahara H., 2013, *PASP*, 65, 16
- Allen S. W., 2000, *MNRAS*, 315, 269
- Allen S. W., Fabian A. C., Johnstone R. M., Arnaud K. A., Nulsen P. E. J., 2001, *MNRAS*, 322, 589
- Allen S. W., Rapetti D. A., Schmidt R. W., Ebeling H., Morris R. G., Fabian A. C., 2008, *MNRAS*, 383, 879
- Andersson K. E., Madejski G. M., 2004, *ApJ*, 607, 190
- Andrade-Santos F., Lima Neto G. B., Laganá T. F., 2012, *ApJ*, 746, 139
- Bahcall N. A., 1977, *ARA&A*, 15, 505
- Baier F. W., Lima Neto G. B., Wipper H., Braun M., 1996, *Astron. Nachr.*, 317, 77
- Barrena R., Boschini W., Girardi M., Spolaor M., 2007, *A&A*, 467, 37
- Barrena R., Girardi M., Boschini W., Dasí M., 2009, *A&A*, 503, 357
- Bauer F. E., Fabian A. C., Sanders J. S., Allen S. W., Johnstone R. M., 2005, *MNRAS*, 359, 1481
- Bautz L. P., Morgan W. W., 1970, *ApJ*, 162, L149
- Belsole E., Pratt G. W., Sauvageot J.-L., Bourdin H., 2004, *A&A*, 415, 821
- Blanton M. R., et al., 2003, *ApJ*, 592, 819
- Bliton M., Rizza E., Burns J. O., Owen F. N., Ledlow M. J., 1998, *MNRAS*, 301, 609
- Böhringer H., et al., 2000a, *ApJS*, 129, 435
- Böhringer H., Soucail G., Mellier Y., Ikebe Y., Schuecker P., 2000b, *A&A*, 353, 124

- Böhringer H., et al., 2004, *A&A*, 425, 367
- Böhringer H., et al., 2010, *A&A*, 514, A32
- Bonafede A., et al., 2012, *MNRAS*, 426, 40
- Boschin W., Barrena R., Girardi M., 2009, *A&A*, 495, 15
- Boschin W., Girardi M., Barrena R., Biviano A., Feretti L., Ramella M., 2004, *A&A*, 416, 839
- Brunetti G., Cassano R., Dolag K., Setti G., 2009, *A&A*, 507, 661
- Buote D. A., 2001, *ApJ*, 553, L15
- Buote D. A., Humphrey P. J., Stocke J. T., 2005, *ApJ*, 630, 750
- Buote D. A., Tsai J. C., 1995, *ApJ*, 452, 522
- Burns J. O., Hallman E. J., Gantner B., Motl P. M., Norman M. L., 2008, *ApJ*, 675, 1125
- Burns J. O., Rhee G., Owen F. N., Pinkney J., 1994, *ApJ*, 423, 94
- Burns J. O., Roettiger K., Pinkney J., Perley R. A., Owen F. N., Voges W., 1995, *ApJ*, 446, 583
- Capelato H. V., Proust D., Lima Neto G. B., Santos W. A., Sodr e Jr., L., 2008, *A&A*, 492, 345
- Cassano R., Etori S., Giacintucci S., Brunetti G., Markevitch M., Venturi T., Gitti M., 2010, *ApJ*, 721, L82
- Chen Y., Reiprich T. H., Böhringer H., Ikebe Y., Zhang Y.-Y., 2007, *A&A*, 466, 805
- Cohen A. S., Clarke T. E., 2011, *AJ*, 141, 149
- Colberg J. M., White S. D. M., Jenkins A., Pearce F. R., 1999, *MNRAS*, 308, 593
- Colless M., Dunn A. M., 1996, *ApJ*, 458, 435
- Comerford J. M., Moustakas L. A., Natarajan P., 2010, *ApJ*, 715, 162
- Cypriano E. S., Lima Neto G. B., Sodr e Jr., L., Kneib J.-P., Camposano L. E., 2005, *ApJ*, 630, 38
- Czoske O., Moore B., Kneib J.-P., Soucail G., 2002, *A&A*, 386, 31
- David L. P., Kempner J., 2004, *ApJ*, 613, 831
- De Filippis E., Schindler S., Castillo-Morales A., 2003, *A&A*, 404, 63
- Donahue M., Voit G. M., O’Dea C. P., Baum S. A., Sparks W. B., 2005, *ApJ*, 630, L13
- Donnelly R. H., Forman W., Jones C., Quintana H., Ramirez A., Churazov E., Gilfanov M., 2001, *ApJ*, 562, 254
- Dressler A., Shectman S. A., 1988, *AJ*, 95, 985
- Durret F., Lima Neto G. B., Forman W., 2005, *A&A*, 432, 809
- Eckert D., Molendi S., Paltani S., 2011, *A&A*, 526, A79
- Edge A. C., Stewart G. C., Fabian A. C., 1992, *MNRAS*, 258, 177
- Einasto M., et al., 2010, *A&A*, 522, A92
- Einasto M., et al., 2012, *A&A*, 540, A123
- Fabian A. C., 1994, *ARA&A*, 32, 277
- Feretti L., Giovannini G., Govoni F., Murgia M., 2012, *A&AR*, 20, 54
- Fisher D., Fabricant D., Franx M., van Dokkum P., 1998, *ApJ*, 498, 195
- Flin P., Krywult J., 2006, *A&A*, 450, 9
- Forman W., Bechtold J., Blair W., Giacconi R., van Speybroeck L., Jones C., 1981, *ApJ*, 243, L133
- Gastaldello F., Trevese D., Vagnetti F., Fusco-Femiano R., 2008, *ApJ*, 673, 176
- Girardi M., Boschin W., Barrena R., 2006, *A&A*, 455, 45
- Govoni F., Ferrari C., Feretti L., Vacca V., Murgia M., Giovannini G., Perley R., Benoist C., 2012, *A&A*, 545, A74
- Govoni F., Markevitch M., Vikhlinin A., van Speybroeck L., Feretti L., Giovannini G., 2004, *ApJ*, 605, 695
- Gutierrez K., Krawczynski H., 2005, *ApJ*, 619, 161
- Halliday C., et al., 2004, *A&A*, 427, 397
- Hao J., et al., 2010, *ApJS*, 191, 254
- Hashimoto Y., Böhringer H., Henry J. P., Hasinger G., Szokoly G., 2007, *A&A*, 467, 485
- Hicks A. K., Mushotzky R., Donahue M., 2010, *ApJ*, 719, 1844
- Holmberg K., Schirmer M., Dahle H., 2009, *A&A*, 504, 1
- Hou A., Parker L. C., Harris W. E., Wilman D. J., 2009, *ApJ*, 702, 1199
- Hou A., et al., 2012, *MNRAS*, 421, 3594
- Hudson D. S., Mittal R., Reiprich T. H., Nulsen P. E. J., Andernach H., Sarazin C. L., 2010, *A&A*, 513, A37
- Jones C., Forman W., 1999, *ApJ*, 511, 65
- Juett A. M., et al., 2008, *ApJ*, 672, 138
- Kale R., Venturi T., Giacintucci S., Dallacasa D., Cassano R., Brunetti G., Macario G., Athreya R., 2013, *A&A*, preprint (arXiv:1306.3102)
- Katgert P., Biviano A., Mazure A., 2004, *ApJ*, 600, 657
- Kempner J. C., Sarazin C. L., Markevitch M., 2003, *ApJ*, 593, 291
- Kempner J. C., Sarazin C. L., Ricker P. M., 2002, *ApJ*, 579, 236
- King I., 1962, *AJ*, 67, 471
- Kneib J. P., Mellier Y., Fort B., Mathez G., 1993, *A&A*, 273, 367
- Kolokotronis V., Basilakos S., Plionis M., Georgantopoulos I., 2001, *MNRAS*, 320, 49
- Liuzzo E., Giovannini G., Giroletti M., Taylor G. B., 2010, *A&A*, 516, A1
- Majerowicz S., Neumann D. M., Romer A. K., Nichol R. C., Burke D. J., Collins C. A., 2004, *A&A*, 425, 15
- Mann A. W., Ebeling H., 2012, *MNRAS*, 420, 2120
- Marini F., et al., 2004, *MNRAS*, 353, 1219
- Markevitch M., Sarazin C. L., Vikhlinin A., 1999, *ApJ*, 521, 526
- Markevitch M., Vikhlinin A., 2001, *ApJ*, 563, 95
- Markevitch M., et al., 2000, *ApJ*, 541, 542
- Maughan B. J., Jones C., Forman W., Van Speybroeck L., 2008, *ApJS*, 174, 117
- Maugordato S., Sauvageot J. L., Bourdin H., Cappi A., Benoist C., Ferrari C., Mars G., Houairi K., 2011, *A&A*, 525, A79
- Medezinski E., Broadhurst T., Umetsu K., Oguri M., Rephaeli Y., Benítez N., 2010, *MNRAS*, 405, 257
- Mohr J. J., Evrard A. E., Fabricant D. G., Geller M. J., 1995, *ApJ*, 447, 8
- Morandi A., Etori S., 2007, *MNRAS*, 380, 1521
- Morrison G. E., Owen F. N., Ledlow M. J., Keel W. C., Hill J. M., Voges W., Herter T., 2003, *ApJS*, 146, 267
- Nuza S. E., Hoefl M., van Weeren R. J., Gottlöber S., Yepes G., 2012, *MNRAS*, 420, 2006
- O’Hara T. B., Mohr J. J., Bialek J. J., Evrard A. E., 2006, *ApJ*, 639, 64
- Ota N., Mitsuda K., 2002, *ApJ*, 567, L23
- Ota N., Mitsuda K., Fukazawa Y., 1998, *ApJ*, 495, 170
- Owers M. S., Nulsen P. E. J., Couch W. J., Markevitch M., 2009, *ApJ*, 704, 1349
- Pedersen K., Dahle H., 2007, *ApJ*, 667, 26
- Peebles P. J. E., 1980, *The Large-Scale Structure of the Universe*. Princeton Univ. Press, Princeton, NJ
- Peterson J. R., Fabian A. C., 2006, *Phys. Rep.*, 427, 1
- Pisani A., 1993, *MNRAS*, 265, 706
- Popesso P., Biviano A., Böhringer H., Romaniello M., 2007, *A&A*, 461, 397
- Popesso P., Böhringer H., Brinkmann J., Voges W., York D. G., 2004, *A&A*, 423, 449
- Puchwein E., Bartelmann M., 2007, *A&A*, 474, 745
- Ramella M., et al., 2007, *A&A*, 470, 39
- Ribeiro A. L. B., Lopes P. A. A., Rembold S. B., 2013, *A&A*, 556, A74

- Richard J., Pei L., Limousin M., Jullo E., Kneib J. P., 2009, *A&A*, 498, 37
- Rood H. J., Sastry G. N., 1971, *PASP*, 83, 313
- Salvador-Sole E., Gonzalez-Casado G., Solanes J. M., 1993, *ApJ*, 410, 1
- Santos J. S., Rosati P., Tozzi P., Böhringer H., Ettori S., Bignamini A., 2008, *A&A*, 483, 35
- Schuecker P., Böhringer H., Reiprich T. H., Feretti L., 2001, *A&A*, 378, 408
- Sehgal N., Hughes J. P., Wittman D., Margoniner V., Tyson J. A., Gee P., dell'Antonio I., 2008, *ApJ*, 673, 163
- Serna A., Gerbal D., 1996, *A&A*, 309, 65
- Shan H., Qin B., Fort B., Tao C., Wu X.-P., Zhao H., 2010, *MNRAS*, 406, 1134
- Sharma M., et al., 2004, *ApJ*, 613, 180
- Shimizu M., Kitayama T., Sasaki S., Suto Y., 2003, *ApJ*, 590, 197
- Smith G. P., Edge A. C., Eke V. R., Nichol R. C., Smail I., Kneib J.-P., 2003, *ApJ*, 590, L79
- Smith G. P., Kneib J.-P., Smail I., Mazzotta P., Ebeling H., Czoske O., 2005, *MNRAS*, 359, 417
- Smith G. P., Taylor J. E., 2008, *ApJ*, 682, L73
- Smith G. P., et al., 2010, *MNRAS*, 409, 169
- Solanes J. M., Salvador-Solé E., González-Casado G., 1999, *A&A*, 343, 733
- Struble M. F., Rood H. J., 1987, *ApJS*, 63, 555
- Sun M., Murray S. S., Markevitch M., Vikhlinin A., 2002, *ApJ*, 565, 867
- Szabo T., Pierpaoli E., Dong F., Pipino A., Gunn J., 2011, *ApJ*, 736, 21
- Tempel E., Tago E., Liivamägi L. J., 2012, *A&A*, 540, A106
- Ulmer M. P., Cruddace R. G., 1982, *ApJ*, 258, 434
- Vacca V., Govoni F., Murgia M., Giovannini G., Feretti L., Tugnoli M., Verheijen M. A., Taylor G. B., 2011, *A&A*, 535, A82
- Venturi T., Giacintucci S., Dallacasa D., Cassano R., Brunetti G., Bardelli S., Setti G., 2008, *A&A*, 484, 327
- Vikhlinin A., Markevitch M., Murray S. S., Jones C., Forman W., Van Speybroeck L., 2005, *ApJ*, 628, 655
- Voigt L. M., Fabian A. C., 2004, *MNRAS*, 347, 1130
- Wang J., Overzier R., Kauffmann G., von der Linden A., Kong X., 2010, *MNRAS*, 401, 433
- Wang Q. D., Ulmer M. P., Lavery R. J., 1997, *MNRAS*, 288, 702
- Weißmann A., Böhringer H., Šuhada R., Ameglio S., 2013, *A&A*, 549, A19
- Wen Z. L., Han J. L., Liu F. S., 2009, *ApJS*, 183, 197
- Wen Z. L., Han J. L., Liu F. S., 2012, *ApJS*, 199, 34
- West M. J., Bothun G. D., 1990, *ApJ*, 350, 36
- West M. J., Oemler Jr., A., Dekel A., 1988, *ApJ*, 327, 1
- Xue S.-J., Wu X.-P., 2002, *ApJ*, 576, 152
- Zhang Y.-Y., Böhringer H., Mellier Y., Soucail G., Forman W., 2005, *A&A*, 429, 85
- Zhang Y.-Y., Finoguenov A., Böhringer H., Kneib J.-P., Smith G. P., Czoske O., Soucail G., 2007, *A&A*, 467, 437
- Zitrin A., Broadhurst T., Bartelmann M., Rephaeli Y., Oguri M., Benítez N., Hao J., Umetsu K., 2012a, *MNRAS*, 423, 2308
- Zitrin A., Bartelmann M., Umetsu K., Oguri M., Broadhurst T., 2012b, *MNRAS*, 426, 2944

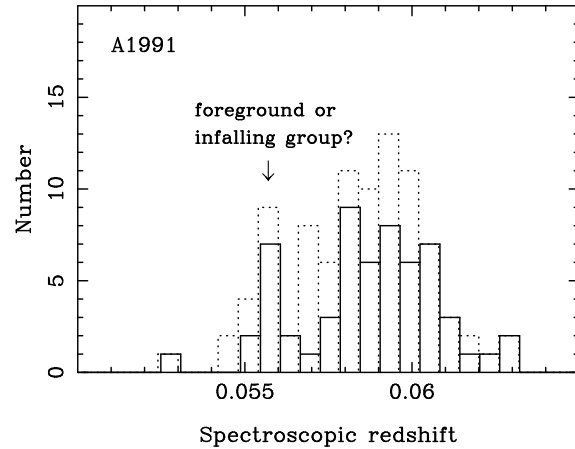


Figure A1. Redshift distribution of member galaxies within r_{200} (dotted line) and r_{500} (solid line) for A1991. The data are extracted from the SDSS-III.

APPENDIX A: FIVE CLUSTERS WITH KNOWN DYNAMICAL STATES BUT UNUSUAL RELAXATION PARAMETERS

Most clusters with known dynamical states can be separated by the plane in Fig. 4 for their relaxed states or unrelaxed states. However, five clusters have unusual relaxation parameters, CL0024.0+1652, A267, A370, A1689, A1991. Here, we investigate them for details.

CL0024.0+1652: we get a relaxation parameter of $\Gamma = 0.49 \pm 0.04$, which means ‘very relaxed’. It has a regular morphology in X-ray image, and does not show a cool core. There is no dominant central galaxy at the center (Böhringer et al. 2000b; Zhang et al. 2005). However, the optical spectroscopic data of member galaxies show a non-Gaussian redshift distribution, which indicates that CL0024.0+1652 is an ongoing merger along the line of sight (Czoske et al. 2002). It is therefore not surprising that the dynamical state of CL0024.0+1652 can not be figured out from optical luminosity distribution of member galaxies.

A267: it has a dominant central galaxy with magnitude difference between the first and second BCGs, $M_{r,2} - M_{r,1} = 2.14$. We get a very regular smoothed optical map and a high relaxation parameter of $\Gamma = 0.48 \pm 0.02$. However, the X-ray and lensing measurements show that A267 has a large offset between the mass centered on BCG and X-ray peak (Smith et al. 2005), which indicates unrelaxed dynamical state of this cluster. No cool core is found (Bauer et al. 2005).

A370: using optical data, we get a relaxation parameter of $\Gamma = 0.07 \pm 0.05$. Ota et al. (1998) suggested that A370 consists of two subclusters in the light-of-sight direction. Two mass clumps are figured out by strong lensing centered on two BCGs with a projected separation of 200 kpc and a velocity difference of about 1000 km s^{-1} (Kneib et al. 1993). X-ray image shows two peaks centered on two BCGs (Shan et al. 2010), and there is no cool core in X-ray (Morandi & Ettori 2007).

A1689: we get a high relaxation parameter of $\Gamma = 0.47 \pm 0.05$, and it shows a regular morphology in X-ray image and looks like a relaxed cluster (Xue & Wu 2002). However, the temperature profiles show evidence for merger along the line of sight (Andersson & Madejski 2004). In X-ray, A1689 has a cool core (Allen 2000; Chen et al. 2007). In radio, a small radio halo has been detected in the central region of this cluster (Vacca et al. 2011).

A1991: using optical photometric data, we get a relaxation pa-

parameter of $\Gamma = -0.41 \pm 0.06$ for this cluster. It has a regular morphology and cool core in X-ray (Vikhlinin et al. 2005; Wang et al. 2010). However, spectroscopic data of member galaxies show the non-Gaussian velocity distribution (see Fig. A1). The feature may suggest that a group is infalling into the cluster (Sharma et al. 2004) or the presence of a possible foreground structure.